



THE HONG KONG
POLYTECHNIC UNIVERSITY

香港理工大學

Pao Yue-kong Library

包玉剛圖書館

Copyright Undertaking

This thesis is protected by copyright, with all rights reserved.

By reading and using the thesis, the reader understands and agrees to the following terms:

1. The reader will abide by the rules and legal ordinances governing copyright regarding the use of the thesis.
2. The reader will use the thesis for the purpose of research or private study only and not for distribution or further reproduction or any other purpose.
3. The reader agrees to indemnify and hold the University harmless from and against any loss, damage, cost, liability or expenses arising from copyright infringement or unauthorized usage.

IMPORTANT

If you have reasons to believe that any materials in this thesis are deemed not suitable to be distributed in this form, or a copyright owner having difficulty with the material being included in our database, please contact lbsys@polyu.edu.hk providing details. The Library will look into your claim and consider taking remedial action upon receipt of the written requests.

**ATOMIC VIEW OF CHALCOGENIDE-
BASED RESISTANCE SWITCHING
MEMORIES**

KO TSZ WAI

MPhil

The Hong Kong Polytechnic University

2019

The Hong Kong Polytechnic University

Department of Applied Physics

**Atomic view of chalcogenide-based
resistance switching memories**

Ko Tsz Wai

A thesis submitted in partial fulfilment of the requirements

for the degree of master of philosophy

Aug 2018



CERTIFICATE OF ORIGINALITY

I hereby declare that this thesis is my own work and that, to the best of my knowledge and belief, it reproduces no material previously published or written, nor material that has been accepted for the award of any other degree or diploma, except where due acknowledgement has been made in the text.

_____ (Signed)

_____ Ko Tsz Wai (Name of student)



Abstract

Resistive random access memories (ReRAM) form a new class of emerging non-volatile memory device foreseen to replace the current Flash technology due to their excellent scalability and low power consumption. ReRAM consist of a solid electrolyte such as chalcogenide glasses or transition metal oxides sandwiched between two metallic electrodes. The operation principle of ReRAM is based on the resistance change of the cell under an applied voltage and the corresponding mechanism often involves the electrochemical formation and dissolution of conductive metallic filaments embedded in the electrolyte. Interestingly, copper-doped germanium-based chalcogenide glasses exhibit two distinct I-V characteristics including bi-polar or uni-polar filamentary switching and threshold switching, depending on the concentration of copper and the composition of the chalcogenide glass. However, the working mechanisms that control switching are not fully understood and are highly dependent on the electrolyte materials. In this study, we propose to explore the optimal composition of the ternary glassy materials Ge-S-Cu for resistance switching by performing molecular dynamics simulations. To achieve this goal, we developed a reactive force field based on a training set of first principle calculations to describe germanium sulfide glass and its interaction with copper. We performed high throughput calculations to generate amorphous structures at various compositions following a melt-and-quench procedure and, we evaluated the corresponding mobility of Cu. Our procedure led to compositions with optimal Cu diffusivity and we studied in details their structural and electronic properties to reveal the atomistic mechanisms of copper diffusion in the glass matrix. We found that high sulfur and copper contents usually lead



to high Cu mobility. Moreover, the glassy mixture is found to be a semiconductor for Cu and S contents lower than 40% and ranging from 30% to 60%, respectively. The highest Cu mobility is predicted for the composition $\text{Ge}_{0.1}\text{S}_{0.8}\text{Cu}_{0.1}$ with an activation energy as low as 0.21 eV. We believe that this work contributes to the general knowledge of metal diffusion in chalcogenide glasses and, can be used to design ultrafast resistance switching devices.



Acknowledgement

I would like to express my sincere gratitude to my chief supervisor, Dr Nicolas Onofrio, he gave me lots of encouragement and support in my academic and personal development. He shared his knowledge, research experience including theories related to my field and techniques for atomistic modelling as well as his constant persistence for me to succeed as a qualified research student. I learn a lot from him, especially on his attitude towards research. In addition, I am grateful to my co-supervisor, Dr C. H. Lam, for his valuable guidance and advice. he gave a great deal of assistance and counselling when I felt stressful and depressed during my research studies.

Also, I would like to express the gratitude to the research groupmate Dr Abhinav Kumar for his useful discussion and support on my research project. Through my MPhil. I am thankful to have studentship support from the Research Grants Council of the Hong Kong Special Administrative Region. Finally, I would like to thank my family, friends, classmates and all the people who supported me in my postgraduate study.



Table of Content

Abstract.....	I
Acknowledgement.....	III
Table of Content.....	IV
List of Figures.....	VI
List of Tables	VIII
List of abbreviations	IX
Chapter 1 Introduction.....	1
Chapter 2 Properties of chalcogenide glasses and their applications.....	6
2.1 Review of chalcogenide glasses	6
2.1.1 Chalcogenide glasses	6
2.1.2 Metal-doped chalcogenide glasses.....	11
2.2 Resistance switching	14
2.2.1 Working principle of ECM cells	16
2.2.2 Working principle of TS	17
Chapter 3 Atomistic Simulations.....	20
3.1 Overview	20
3.2 Density functional theory	21
3.2.1 Exchange-correlation potentials	22
3.2.2 A practical view of DFT	23
3.2.3 Molecular dynamics	25
3.3 Classical molecular dynamics	26
3.3.1 Traditional empirical interatomic potentials.....	26
3.3.2 Reactive force fields	29
Chapter 4 Development of ReaxFF for Ge/S/Cu elements.....	32
4.1 Overview	32
4.2 Methodology and simulation details.....	32
4.2.1 Training set	32



4.2.2 Optimization algorithm	35
4.2.3 Validation procedures.....	37
4.2.4 Structural analysis.....	38
4.3 Results and discussion	38
4.3.1 Force field optimization	38
4.3.1.1 Amorphous structures	38
4.3.1.2 Small molecules.....	40
4.3.1.3 Crystals	41
4.3.1.4 Clusters	44
4.3.2 Validations	44
4.3.2.1 Germanium sulfide glasses	44
4.3.2.2 Copper doped germanium sulfide glasses	50
Chapter 5 Exploring the compositions of $\text{Ge}_x\text{S}_y\text{Cu}_z$ for resistance switching..	54
5.1 Overview	54
5.2 Stimulation details.....	54
5.3 Results and discussions	56
5.3.1 Activation energy.....	56
5.3.2 Electronic bandgap	58
5.3.3 The normalized cluster size of copper	59
Chapter 6 Conclusions and Future work.....	62
6.1 Conclusions	62
6.2 Future work	63
References.....	64



List of Figures

Figure 1.1. Hierarchy of conventional memory devices showing a gap of approximately 3 orders of magnitude in access time.	2
Figure 2.1. Volume versus temperature for both glasses and crystals (adapted from Ref. [19]).....	6
Figure 2.2. Total and partial RDF of amorphous GeS ₂ structures (adapted from Ref. [21] and Ref. [22]).	8
Figure 2.3. Structure of edge-sharing GeS ₄ tetrahedra and corner-sharing GeS ₄ tetrahedra.....	9
Figure 2.4. Total RDF (left) and fraction of the edge-sharing GeS ₄ (right) for selected GeS _x glasses (adapted from Ref. [20]).....	9
Figure 2.5. (left) Comparison of total RDF in amorphous germanium sulfide glasses between FPMD [27] and neutron diffraction experiment (GeS ₉ [20], GeS ₄ [26], GeS ₂ (circle [28] and purple [29]), GeS _{1.5} [28]) (right) Recent FPMD simulation results of total RDF in GeS ₂ [21, 23, 27, 30] and GeS ₄ [26, 27]. The percentage mentioned in different curve represents the content of Ge in the germanium sulfide glasses Ge _x S _{1-x}	10
Figure 2.6. Temperature-dependent diffusion coefficients of Cu in (left) GeS ₃ and (Middle) GeS ₆ . Blue and orange filled circles correspond to the copper content of 5% and 20%, respectively. (right) The activation energy for diffusion of Copper in GeS ₃ and GeS ₆ for the content of 5% and 20% Cu (adapted from Ref. [25]).	12
Figure 2.7. Working mechanism of an ECM cell at different stages during switching (adapted from Ref. [12]).	16
Figure 2.8. The working mechanism, corresponding simulated and experimental I-V characteristics of MIEC-based TS (adapted from Ref. [49]).	19
Figure 3.1. Multi-scale modelling techniques for atomistic simulations.....	20
Figure 4.1. The training set for optimizing the ReaxFF including Ge, S and Cu	33
Figure 4.2. The procedures for optimizing the ReaxFF based on the algorithm	35
Figure 4.3. (a) The relation between energy and interatomic distance during bond dissociation of S=S, S-S, S-H,(b) Ge-Ge, Ge-S and Ge=S bond (c) relation between energy and various angle bending/dihedral angle torsion of some small molecules included in the training set computed with optimized ReaxFF (blue) and DFT (red).	40
Figure 4.4. Energy curve for the EOS of the (a) various crystal phases of Cu, (b) crystals GeS and GeS ₂ , (c) CuGe ₃ , Cu ₃ Ge and CuS ₂ , (d) Cu ₂ GeS ₃ and Cu ₂ GeS ₄ with isotropic deformation. The minimum energy of EOS is shifted to their corresponding cohesive/formation energy.	43



Figure 4.5. Comparison between total and partial radial distribution functions of amorphous GeS ₂ averaged over 10 and 5 samples computed by DFT, the optimized ReaxFF with FPMD [21].	46
Figure 4.6. Comparison of total structure factor of amorphous GeS ₂ averaged over 10 and 5 samples computed by DFT, the optimized ReaxFF with FPMD [21].	47
Figure 4.7. Comparison of defect distributions of amorphous GeS ₂ averaged over 10 and 5 samples computed by DFT, the optimized ReaxFF with FPMD [21].	47
Figure 4.8. Total and partial RDF of amorphous GeS ₃ and GeS ₆ averaged over 5 samples computed by ReaxFF and FPMD [25].	49
Figure 4.9. The coordination number of Ge-S in glassy GeS ₃ and GeS ₆ averaged over 5 samples generated by the ReaxFF and FPMD [25].	49
Figure 4.10. the averaged atomic density of (GeS ₃) _{1-x} Cu _x and (GeS ₆) _{1-x} Cu _x with x = 5%, 20%, 25%, 35% and 50% generated by ReaxFF and FPMD [25].	50
Figure 4.11. The averaged total RDF of (GeS ₃) _{1-x} Cu _x and (GeS ₆) _{1-x} Cu _x with x = 5%, 20% generated by ReaxFF and FPMD [25].	51
Figure 4.12. Coordination of Ge-S for (GeS ₃) _{1-x} Cu _x and (GeS ₆) _{1-x} Cu _x systems with x = 5% and 20% and FPMD [25].	52
Figure 4.13. Temperature-dependent diffusion coefficients of Cu in (left) GeS ₃ and (Middle) GeS ₆ with 5% and 20% content of Cu generated by ReaxFF.	53
Figure 5.1. The procedures for calculating activation energy for Cu diffusion in the copper-doped germanium glasses at various compositions.	55
Figure 5.2. Ternary diagram for activation energy of Cu diffusion in amorphous Ge _x S _y Cu _z at various compositions.	56
Figure 5.3. Averaged coordination number distribution of Cu atoms at glassy Ge _{0.1} S _{0.8} Cu _{0.1} and Ge _{0.1} S _{0.4} Cu _{0.5} .	57
Figure 5.4. Ternary diagram for electronic bandgap of amorphous Ge _x S _y Cu _z at various compositions	58
Figure 5.5. Total and partial density of state projected on germanium, sulfur and copper atoms for Ge _{0.3} S _{0.6} Cu _{0.1} , Ge _{0.2} S _{0.4} Cu _{0.4} and Ge _{0.1} S _{0.2} Cu _{0.7} glasses. The Fermi energy (E _f) has been shifted to zero for all compositions.	59
Figure 5.6. Ternary diagram for a normalized cluster size of Cu in amorphous Ge _x S _y Cu _z at various compositions.	60
Figure 5.7. Atomic configuration and Normalized cluster size of Cu atom for Ge _{0.3} S _{0.6} Cu _{0.1} , Ge _{0.2} S _{0.4} Cu _{0.4} and Ge _{0.1} S _{0.2} Cu _{0.7} glasses.	60



List of Tables

Table 1.1. Comparing the Novel and current memory and storage technologies (adapted from Ref. [10]).....	3
Table 2.1. Coordination number and pair coordination number of $\text{Ge}_x\text{S}_{1-x}$ for $10\% < x < 40\%$ (adapted from Ref. [27]).....	11
Table 2.2. Comparison between ECM cells and TS devices composition, mechanisms and switching characteristics.	15
Table 4.1. Comparison of mean absolute error for charge (e/atom) by computing with DFT and ReaxFF for different amorphous structures.	39
Table 4.2. Cohesive energy corresponding to reactions with over-coordinated S atoms as well as some small cyclic sulfur cluster. All the units for energies were reported in kcal/mol/atom of the reactant.....	41
Table 4.3. Cohesive energy (kcal/mol/atom) for unary crystals and, formation energy (kcal/mol/atom) for binary and ternary crystals, mean absolute error for energy (kcal/mol/atom) and charges (e/atom) based on the DFT optimized structure computed with DFT and ReaxFF for various crystals. Materials project IDs and the nearest neighbour partial coordination were also provided. Additional data were included to demonstrate the transferability of the optimized parameters.	42
Table 4.4. Cohesive energy of small CuS clusters computed with DFT and the optimized ReaxFF (in kcal/mol/atom).	44
Table 4.5. The mean and standard deviation of the calculated atomic density for amorphous GeS_2	45
Table 4.6. The mean and standard deviation of the atomic density for amorphous GeS_3 and GeS_6	48
Table 4.7. Activation energy of copper diffusion in GeS_3 and GeS_6 with 5% and 20% content of Cu by FPMD [25]) and ReaxFF.....	53



List of abbreviations

B3LYP	Becke 3 Yang and Parr exchange-correlation functional
CG	Chalcogenide glasses
DFT	Density functional theory
DOS	Density of state
DRAM	Dynamic random access memory
ECM	Electrochemical metallization
FPMD	First principle molecular dynamics
GGA	Generalized gradient approximation
HRS and LRS	High resistance state and Low resistance state
HSE	Heyd-Scuseria-Ernzerhof exchange-correlation functional
LAMMPS	Large-scale Atomic/Molecular Massively Simulator
LDA	Local density approximation
MD	Molecular dynamics
MM	Molecular Mechanics
ORCA	An ab initio, DFT and semiempirical SCF-MO package
PAW	Projector Augmented Wave
PBE	Perdew Burke Ernzerhf exchange-correlation functional
PCM	Phase change memory
PES	Potential energy surface
QEq	Charge equilibration
QM	Quantum Mechanics
RDF	Radial distribution function
ReaxFF	Reactive force field
SCF	Self-Consistent-Field
STT-RAM	Spin Torque Transfer Random access memory
TS	Threshold switching
VASP	Vienna Ab initio simulation package
EOS	Equation of state



Chapter 1 Introduction

Over the past decades, personal electronics have undergone significant advances; this includes computers with more powerful processing capacities and ever large data storage [1]. To satisfy Moore's law, the dimensions of the electronic components including microprocessor and memory are pushed towards the sub-10nm regime and traditional scaling methods of the semiconductor industry face technological and fundamental challenges [2]. Therefore, it is vital to develop novel and original technology to pursue miniaturization. Emerging device operations such as nanoscale resistance switch, for non-volatile memory application, has the potential to contribute to the extension of Moore's law beyond the rapidly approaching end of scaling.

Many metal-insulator-metal systems show electrically induced resistive switching effects and have been proposed as the basis for future non-volatile memories [3]. Resistive memories combine the advantages of Flash and DRAM [4] while avoiding their drawbacks [1]. For instance, DRAM access is measured as fast as 30 ns and endurance up to 10^{15} cycles. By contrast, Flash access is approximately 1 μ s with low endurance corresponding to 10^6 cycles. However, the cost of the DRAM is much higher than Flash. Hence, there is a gap in the conventional memory hierarchy [5] as shown in Figure 1.1

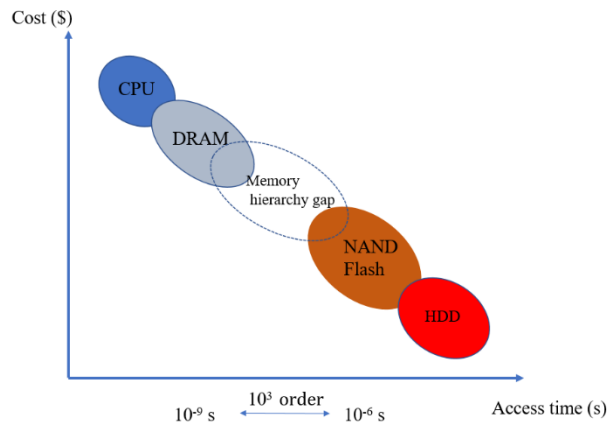


Figure 1.1. Hierarchy of conventional memory devices showing a gap of approximately 3 orders of magnitude in access time.

To fill the memory gap, researchers have recently proposed four types of resistive switch-based devices including PCM [6], ECM cells [7], STT-RAM [8] and TS [9]. The switching mechanism of PCM is based on the phase transition between amorphous and crystal state while STT-RAM is based on the relative orientation of the magnetization of the two magnetic electrodes. Besides, the working mechanism of ECM cells and TS is related to the migration of cations. Surprisingly, the general structure of these devices is similar and consists of a solid electrolyte sandwiched between two metallic electrodes [7]. For reference, we show Table 1.1 the performance of commercial and novel memory storage technology, adapted from Ref. [10].

*Table 1.1. Comparing the Novel and current memory and storage technologies (adapted from Ref. [10])*

	DRAM	FLASH	RRAM	PCM	STTRAM
	Current			Novel	
Cell size (F ²)	6-12	1-4	< 4	4-16	20-60
Energy per bit (pj)	0.005	0.00002	0.1-0.3	2-25	0.1-2.5
Read time (ns)	10	10 ⁵	< 10	10-50	10-35
Write time (ns)	10	10 ⁵	~ 10	50-500	10-90
Retention	<< second	Years	years	years	years
Endurance (cycles)	>10 ¹⁶	10 ⁴	10 ¹²	10 ⁹	10 ¹⁵

Resistive switch-based memory devices share some common features of operation. For instance, they are non-volatile two-terminal devices and they differentiate their states by the switching between a low resistance state (LRS or on state and a high resistant state (HRS, or off state) under an applied voltage [11]. By contrast to their simple structure, the mechanisms that govern switching are rich and complex leading to a variety of electrical characteristics including linear to non-linear bipolar resistance and non-polar resistance switching. Interestingly, the same materials have been used as electrolytes across the different classes of resistance switching devices. For instance, metal-doped chalcogenide glasses (CG) [12] have been demonstrated as an effective electrolyte for applications as both ECM cells and TS devices due to their lower electronic band gap and higher cation diffusion in the glasses compared with transition metal oxide glasses [13], More recently, metal doped oxides have also been used as an



electrolyte for both ECM and TS devices [14]. However, the relationship between composition and the electrochemical response of the cells is still unclear. One of the major challenges for improving the switching characteristics is to find the optimal composition of the electrolyte. Different composition of the solid electrolyte can dramatically affect the atomic mechanism of switching and therefore exhibit the different electrical response of the cell.

Recent experimental studies based on high-resolution transmission electron microscopy imaging [15] and scanning tunnelling microscopy [16, 17] are providing key insights and quantitative information regarding the fundamental physics of these devices; however, these techniques have some limitations, especially when dealing with devices at their miniaturization limit (i.e. few nanometers) and operating at ultra-fast speed (i.e. nanoseconds). Interestingly, the spatial and temporal scales involved make the problem amenable to molecular dynamics (MD) simulations which, in principle, has the potential to provide the full atomistic picture of their operation. In addition, using classical MD to generate atomic structures of amorphous solid electrolyte would allow a fast and efficient search for optimal compositions. Unfortunately, there is currently no accurate force field describing the interactions between a metal and CG. Therefore, the objectives of this thesis are formulated as follows:



- i. The development of a reactive force field for metal-doped CG (Ge, S and Cu); it is computationally efficient with high chemical accuracy for performing high throughput molecular dynamics simulations to explore the compositions for ultra-fast resistance switching.
- ii. The study of an ensemble of Cu-doped germanium sulfide glasses at various compositions to explore various solid electrolytes for resistive switching; the relationship between compositions and structural properties is still not well known. Therefore, this work sheds light on the prediction of physical and electronic properties at various compositions.
- iii. The investigation of the atomic mechanism of copper diffusion in the chalcogenide glasses matrix. Copper Diffusion in the electrolyte plays an important role to achieve the ultra-fast resistance switching. This work provides the defect analysis and cluster size analysis in order to evaluate the diffusion of Cu atoms.

Chapter 2 Properties of chalcogenide glasses and their applications

2.1 Review of chalcogenide glasses

2.1.1 Chalcogenide glasses

CGs are promising amorphous semiconducting materials formed by the combination of S, Se and Te and, elements such as Ge, As, Sb, Ga [18] and they exhibit outstanding flexibility in terms of physical and electronic properties depending on the chemical compositions. The formation of CGs can be obtained by a melt and quench procedure.

Figure 2.1. shows the impact of temperature on the volume of the glass-forming material during the quenching procedure.

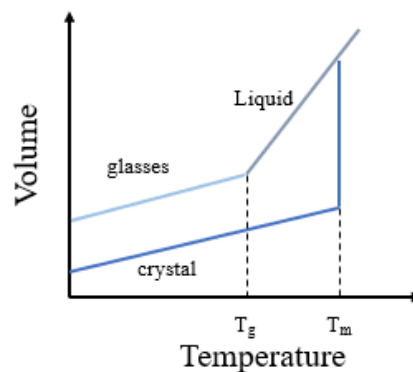


Figure 2.1. Volume versus temperature for both glasses and crystals (adapted from Ref. [19]).

When a stable liquid system is quenched to below its melting point (T_m) with very fast cooling rate, the super-cooled liquid system doesn't have enough time to let atoms explore the configurational space and undergo crystallization. After further cooling with slower quenching rate at the glass transition temperature (T_g), the system solidifies into an amorphous state and the corresponding volume is different with crystal state.



Significant efforts have been devoted to studying the structural and electronic properties of CGs by experimental measurement and first principle molecular dynamics (FPMD) simulation. Amorphous GeS₂ is a common CGs and the corresponding structural properties can be characterized by its radial distribution function (RDF) [20]. The total RDF is defined as the probability to find an atom in a shell at the distance of reference atom while partial RDF $g_{\alpha\beta}$ gives the density probability of an atom of the α species to have a neighbor of the β species at a given distance r .

$$g_{\alpha\beta}(r) = \frac{dn_{\alpha\beta}(r)}{4\pi r^2 dr \rho_{\alpha}} \text{ with } \rho_{\alpha} = \frac{V}{N_{\alpha}} = \frac{V}{N \times c_{\alpha}} \quad (2.1)$$

where $dn_{\alpha\beta}(r)$ represents the number of the atomic species β at a distance between r and $r + dr$ from atomic species α , c_{α} and N represents the concentration of species α and total number of atoms, V represents the volume of the shell with thickness dr . Figure 2.2. shows total and partial RDF for a typical sample of amorphous GeS₂.

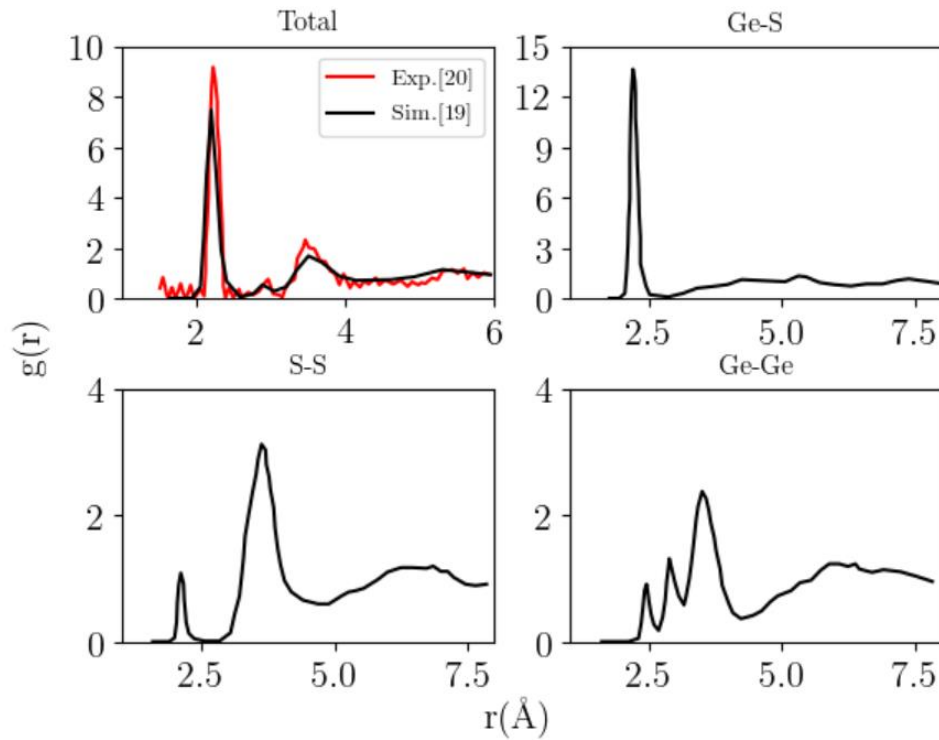


Figure 2.2. Total and partial RDF of amorphous GeS_2 structures (adapted from Ref. [21] and Ref. [22]).

From the simulation and experimental results, the location of the first peak at $\approx 2.2 \text{ \AA}$ and second peak at $\approx 2.9 \text{ \AA}$ of total RDF corresponds to the bond length of Ge-S and distance between Ge-Ge in edge-sharing GeS_4 tetrahedra respectively. The position of the third broad peak at $\approx 3.5 \text{ \AA}$ corresponds to S-S second neighbour and distance between Ge-Ge in corner-sharing GeS_4 tetrahedra. Figure 2.3 shows the structure of edge-sharing GeS_4 and corner-sharing GeS_4 .

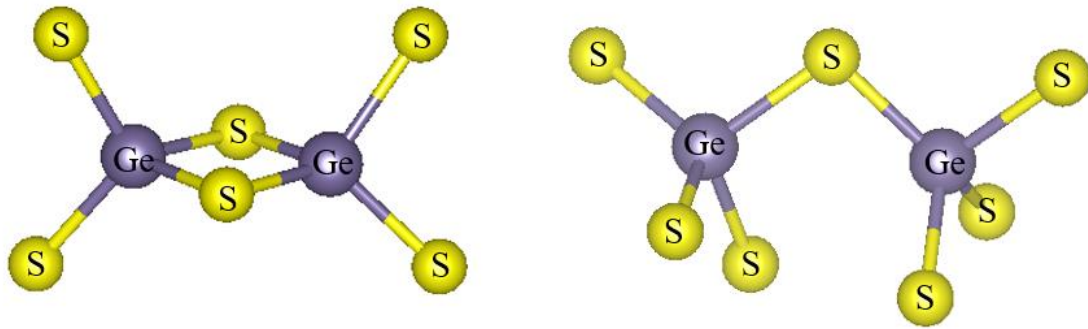


Figure 2.3. Structure of edge-sharing GeS_4 tetrahedra and corner-sharing GeS_4 tetrahedra.

In addition, the bond length between Ge and S, S and S, Ge and Ge can be extracted from the first peak at 2.19 Å, 2.43 Å and 2.11 Å of the corresponding partial RDF.

Figure 2.4. shows the total correlation function which is defined as the total RDF and fraction of edge-sharing GeS_4 tetrahedra when ranging from GeS_2 to GeS_9 , characterized by neutron and X-ray diffraction measurement [20].

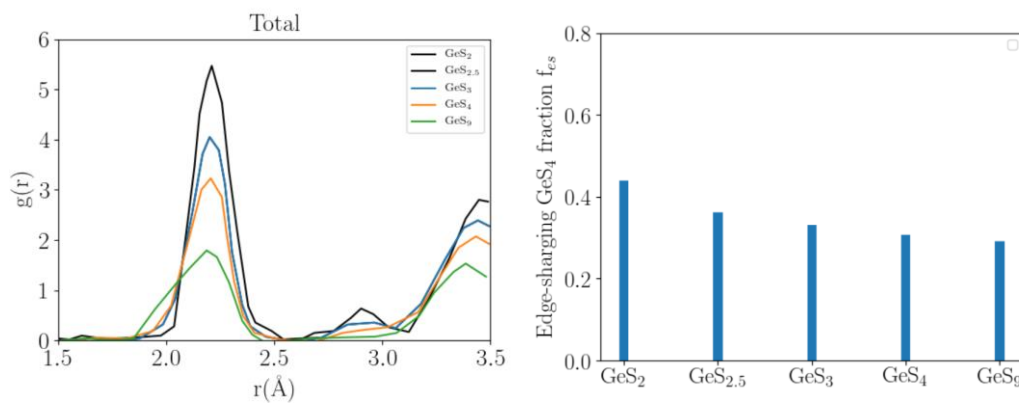


Figure 2.4. Total RDF (left) and fraction of the edge-sharing GeS_4 (right) for selected GeS_x glasses (adapted from Ref. [20]).

The peak of S-S correlation at 2.04 Å is rising while the peak of Ge-Ge correlation at 2.89 Å is declining with the edge-sharing GeS_4 fraction when ranging from GeS_2 to GeS_9 , it implies that the excessive sulfur atoms preferred to form sulfur dimers or short



chains than corner-sharing GeS_4 between stoichiometric GeS_2 and saturated compositions $\text{GeS}_{2.7}$. If the concentration of sulfur is larger than the saturated compositions, longer sulfur chains will be formed in the glass network. Recent work has been focused on amorphous germanium sulfide structures at particular compositions including GeS_2 [21, 23, 24], GeS_3 [25], GeS_4 [26] and $\text{Ge}_x\text{S}_{1-x}$ [27] for $10\% < x < 40\%$ via FPMD simulations. Figure 2.5. shows the total RDF in germanium sulfide glasses with selected compositions at 300K generated by FPMD simulations and neutron diffraction experiments in recent literature.

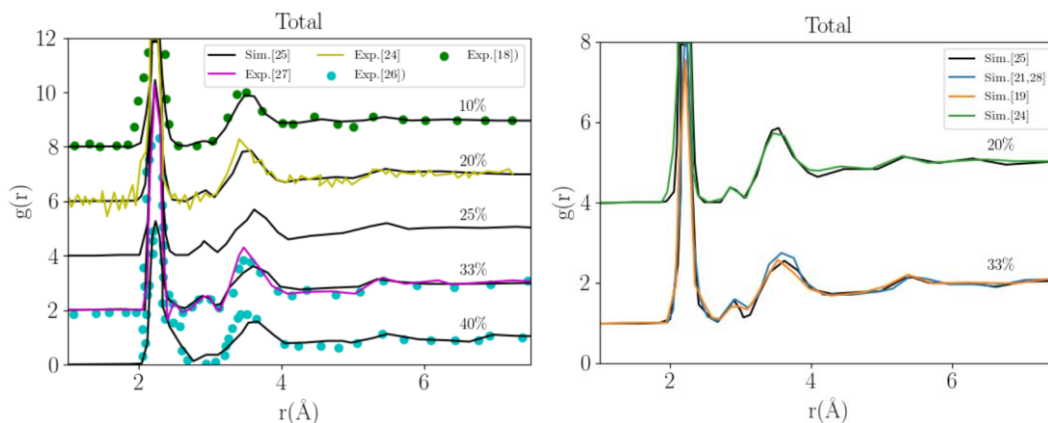


Figure 2.5. (left) Comparison of total RDF in amorphous germanium sulfide glasses between FPMD [27] and neutron diffraction experiment (GeS_3 [20], GeS_4 [26], GeS_2 (circle [28] and purple [29]), $\text{GeS}_{1.5}$ [28]) (right) Recent FPMD simulation results of total RDF in GeS_2 [21, 23, 27, 30] and GeS_4 [26, 27]. The percentage mentioned in different curve represents the content of Ge in the germanium sulfide glasses $\text{Ge}_x\text{S}_{1-x}$.

Both FPMD results are able to reproduce all the experimental features including the number and position of relevant peak. The pair coordination number n_{ij} and



coordination number n_i of $\text{Ge}_x\text{S}_{1-x}$ for $10\% < x < 40\%$ defined from the location of the peaks of partial RDF ($r_{\text{cut-off}} = 2.6\text{-}2.9 \text{ \AA}$) are shown in table 2.1.

Table 2.1. Coordination number and pair coordination number of $\text{Ge}_x\text{S}_{1-x}$ for $10\% < x < 40\%$ (adapted from Ref. [27]).

	n_{GeGe}	n_{GeS}	n_{SS}	n_{Ge}	n_{S}
GeS₉		4.00	1.56	4.00	2.20
GeS₄		3.96	1.0	3.96	2.38
GeS₃		3.99	0.67	3.99	2.50
GeS₂	0.1	3.85	0.10	3.95	2.67
GeS_{1.5}	0.37	3.24		3.57	2.72

The pair coordination number n_{GeS} decreases rapidly from 3.85 to 3.24 when the content of Ge ranges from 33% to 40% due to the emergence of homopolar Ge-Ge bonds and coordination defect. Similarly, n_{SS} slightly increases with the content of germanium due to the emergence of threefold sulfur coordination.

2.1.2 Metal-doped chalcogenide glasses

In addition to binary CGs, metal-doped CGs have drawn great attention from researchers due to their remarkable structural and electronic properties. For instance, the conductivity and silver diffusion in glassy $\text{Ag}_x\text{Ge}_y\text{S}_z$ with the silver concentration ranging between $0.008\% \leq x \leq 25\%$ were studied by tracer diffusion measurement



[31]. They found that the activation energy of Ag diffusion in germanium sulfide glasses decreases from 0.89 to 0.39 eV with a concentration of Ag ranging from 0.008 to 25%. This study shows that metal doping can dramatically change the ion diffusion of copper in CGs. Metal-doped CGs were also investigated by FPMD simulations in recent year. For instance, the temperature-dependent diffusion coefficient of copper in amorphous GeS_3 and GeS_6 at various Cu content were investigated by FPMD [25]. Figure 2.6 shows the temperature-dependent coefficient of Cu for glassy GeS_3 and GeS_6 with the 5% and 20% content of Cu and corresponding activation energy of for diffusion of copper.

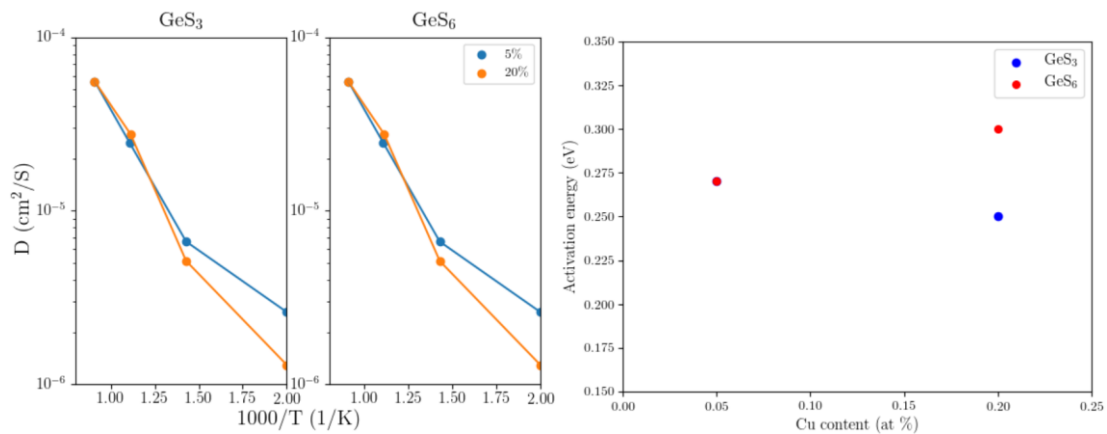


Figure 2.6. Temperature-dependent diffusion coefficients of Cu in (left) GeS_3 and (Middle) GeS_6 . Blue and orange filled circles correspond to the copper content of 5% and 20%, respectively. (right) The activation energy for diffusion of Copper in GeS_3 and GeS_6 for the content of 5% and 20% Cu (adapted from Ref. [25]).

The MSD is calculated and averaged by the last 30ps of the simulation according to the equation:



$$MSD(t) = \langle (r(t)^2 - r(0)^2) \rangle \quad (2.2)$$

where $r(t)$ represents the position of Copper atoms at time t . The temperature-dependent diffusion coefficient is extracted by performing the linear fit for the tail of the MSD curve based on the equation:

$$MSD(t) = 6Dt \quad (2.3)$$

Where D and t describe the temperature-dependent diffusion coefficient and time respectively, Finally, we evaluated the activation energy based on the Arrhenius equation:

$$D = D_0 e^{\frac{-E_a}{k_B T}} \quad (2.4)$$

Where D_0 , E_a , k_B and T represent temperature-independent preexponential, activation energy for the copper diffusion and temperature respectively. Practically, we extracted the activation energy by taking natural logarithm to the both sides and finally performing the linear fit with 4 diffusion coefficients. The activation energy for diffusion of copper in the S-rich germanium sulfide glasses was predicted to be 0.2 to 0.3 eV and the concentration of copper didn't have a significant effect on the diffusivity of Cu atom. CGs and metal doped CGs represent good candidates for dielectrics in metal/insulator/metal devices such as the one presented below.

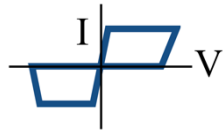
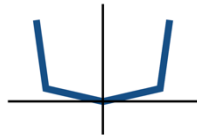


2.2 Resistance switching

Resistance switching exhibits a wide range of applications including logic operations and memory devices [32] and their working principle is based on switching between high resistance state and low resistance state under an external electric field. Interestingly, the switching process is reversible and nonvolatile. Therefore, resistance switching has been widely studied for designing novel memory devices including phase change memory [33] and ECM cells [34, 35]. Recently, ECM cells have been assembled in 3D stack arrays and various methods have been introduced in order to access the memory element while limiting leakage currents to the surrounding elements [7] for achieving high-density memory. For instance, ECM cells can be coupled with a TS device that will act as a selector, and following this principle, Micron and Intel have introduced the 3D Xpoint array [36] in 2015. Presently, resistive memories are widely developed for data storage and information processing. It can be leveraged across memory hierarchy between the DRAM and Flash memories [37]. The goal of the thesis is to understand better the relationship between mechanism and composition of ECM cells and TS devices. The structure of both devices are similar and composed of a solid electrolyte sandwiched between two electrodes. ECM cells require an electroactive electrode material to enable dissolution of metal ions whereas TS devices are made of a solid electrolyte that already contains mobile ions. In this Chapter, we will discuss the

proposed mechanisms for ECM and TS operation. Table 2.2 compares the ECM and TS devices operation including various references.

Table 2.2. Comparison between ECM cells and TS devices composition, mechanisms and switching characteristics.

Resistance switching device	Solid electrolyte	Working Mechanism	I-V signal
Electrochemical metallization cells	SiO ₂ [38], ZnO [39], GeS _x [40], GeSe [41], GeS [42], GeTe [43]	Mostly filamentary [16-20]	
Threshold switch	SiO ₂ /Cu [44], SiO ₂ /Ag [45], Al ₂₀ As _x Te _{80-x} [46], GeS [47], GeSe [48]	Fast reorganization of metal ions and vacancies [49] Sometimes filamentary [44]	

Metal-doped Chalcogenide glasses can be the efficient solid electrolyte material for ECM cells and TS. The metal provides the structural flexibility required for ECM cells at the lower content of metal. In addition, the structural connectivity of the glasses increases at higher concentration of the metal that is more difficult for structural reorganization and eventually leading threshold behaviour [50].

2.2.1 Working principle of ECM cells

Switching in ECM cell is non-volatile, reversible and the change in the resistance state of the devices is used as a basis to store information. ECM cells are composed of a solid electrolyte (i.e. CG or an oxide) sandwiched between an active anode (made of Cu or Ag) and an inert cathode (often made of Pt) [7]. When a positive voltage is applied to the anode; its composing atoms undergo an oxidation reaction and dissolve into the solid electrolyte. The dissolved ions are electric field driven toward the cathode and, nucleate inside the solid electrolyte or are the cathode/electrolyte interface. This electrochemical process eventually leads to the formation of a highly conductive metallic filament that can bridge the electrodes, at the origin of the resistance switching of the device now in the low resistance state (or ON state). When the applied voltage is reversed, the metallic filament dissolves and the device returns to its initial high resistance state (OFF state) [12]. Figure 2.7. summarizes the operation of an ECM cell.

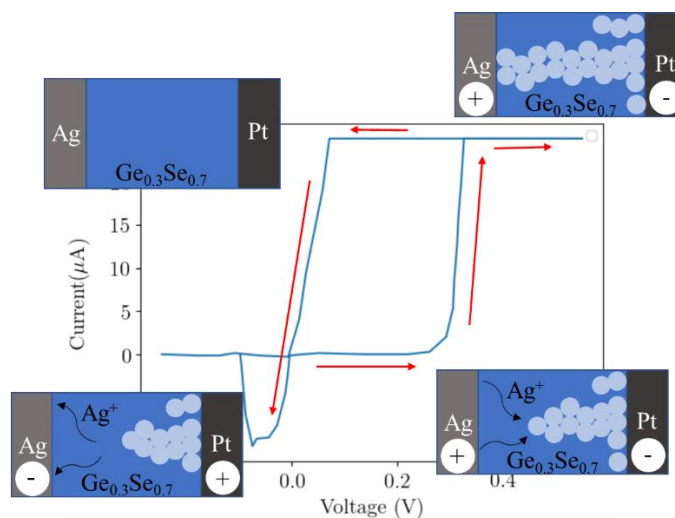


Figure 2.7. Working mechanism of an ECM cell at different stages during switching (adapted from Ref. [12]).



ECM cells have excellent performance characteristics for memory technologies. For instance, switching speed has been measured as fast as 50 ns [11]. Low power consumption reported to be 0.1 pJ/bit [11] with voltage operation as low as few meV. In addition, the endurance of devices has been measured up to 10^{11} , the cell area can be reduced to less than 10 nm and high on/off ratio have been reported of 10^4 [11]. To conclude, ECM cells show strength required for emerging non-volatile memory technologies and there is no doubt these devices will be part of the future memory zoo. Recently, emerging CG based ECM memory cells are predicted to replace the current Flash technology because of their ultra-fast operation speed, exceptionally large ON/OFF ratio and excellent scalability. They can be investigated by experimental methods such as atomic force microscopy (AFM) [7] and transmission electron microscopy (TEM) imaging [15] and they are able to provide the information including the formation and dissociation of metallic filament during the device operation.

2.2.2 Working principle of TS

The I-V characteristics of TS (also called “selector” or “access device”) are similar to that of a diode. When the applied voltage is less than the threshold voltage, the current is nearly equal to zero and the device remains in a high resistivity state (HRS). Once the applied voltage is larger than the threshold voltage, the current will dramatically increase and the device switches to a low resistance state. Finally, the devices will



restore its HRS when the applied voltage reduces below the threshold voltage. Mixed ionic-electronic (MIEC)-based TS represents an important component for producing resistive memory devices with crossbar structure since it enables the memory cell (e.g. ECM cells or phase change memory) to be written or read without requiring a transistor. MIEC-based TS is composed of a solid electrolyte (i.e. metal doped CG or an oxide) sandwiched between two inert electrodes.

The simulations of MIEC-based TS with Cu doped materials were performed to explain the working mechanism of the device operation [49]. Under no applied voltage the metal ions settle at the interfaces maintaining a dynamic equilibrium between ion diffusion and ion drift from each interface. The metal ion accumulation will create the narrow depletion region and residual electron tunnelling at each interface. When the voltage increases, metallic ions move away from the positive electrode and vacancies move toward the positive electrode, eventually leading to an exponentially increase in hole current where the threshold voltage of devices depends on material bandgap. The high concentration of metal ions in the solid electrolyte does not form filaments for devices with a large electrode gap. Interestingly, if the area of the electrodes is not the same (i.e large versus small area), the filamentary process can overcome the electronic flow. Figure 2.8. summarizes the operation and corresponding I-V characteristics of a TS.

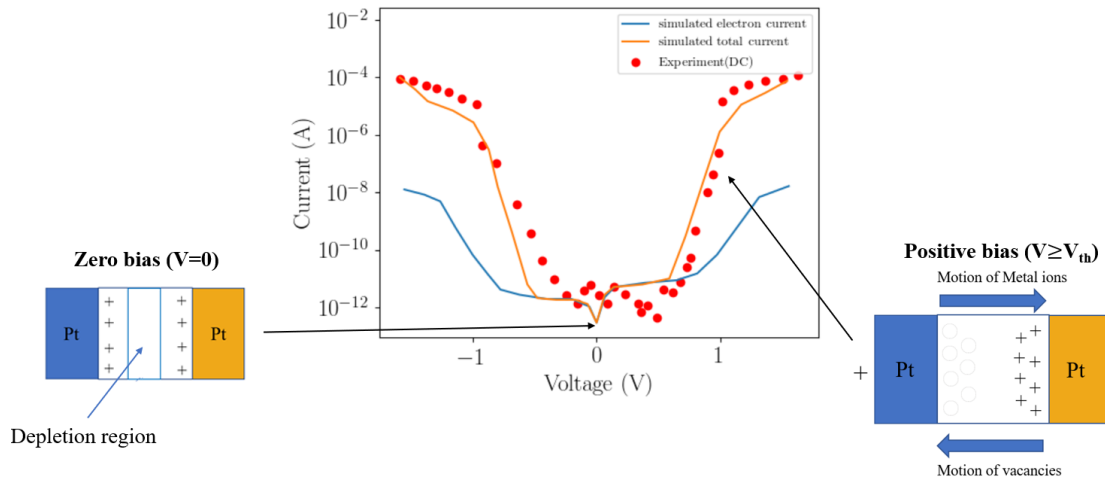


Figure 2.8. The working mechanism, corresponding simulated and experimental I-V characteristics of MIEC-based TS (adapted from Ref. [49]).

Recently, the doping effect of metal ions on thermally evaporated solid electrolyte materials of ECM cells are studied that the device exhibit breakdown diode-like and bipolar resistive memory switching I-V characteristic [44]. More precisely, the device exhibits a TS behaviour due to the breaking of the metallic filament spontaneously at small voltage value. On the other hand, the bi-polar memory switching behaviour of the device can be attributed to the suppression of Cu diffusion and elimination of moisture generated by the electric field in the porous solid electrolyte materials matrix. This last study demonstrates how compositions-dependent TS and ECM mechanisms are similar and not fully understood. Simulation methods such as the one proposed in this thesis will help to answer this question by exploring the compositions of copper-doped germanium sulfide glasses for ECM cells and TS.



Chapter 3 Atomistic Simulations

3.1 Overview

Molecular modelling is a powerful technique for scientists to predict and observe the properties of materials. Atomistic methods are either based on QM or MM and enable various time and length scales. QM-based (also called *ab initio* or first principle) methods provide a numerical evaluation of the electronic wave function (or density) of the system, solution of the Schrödinger equation. QM methods include Hartree-Fock and DFT, enable simulations of hundreds of atoms up to tens of picoseconds. MM methods are less accurate and based on an approximation of the interaction between atoms mapped into an empirical interatomic potential. MM methods enable multi-million atoms simulations up to the microsecond timescale. Therefore, the choice of the atomistic method relies on a compromise between the accuracy and the scales covered by the simulations. Figure 3.1 show atomistic methods and the corresponding length and time scales covered.

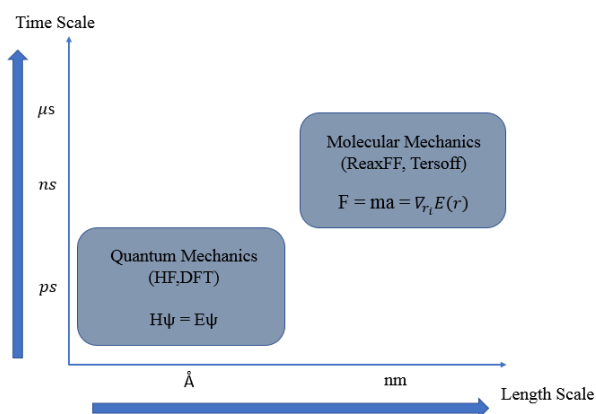


Figure 3.1. Multi-scale modelling techniques for atomistic simulations.



In the proposed study, we want to simulate an ensemble of amorphous structures with different compositions. The generation of amorphous structures based on first principle methods is highly computer demanding and, only possible for small samples. Therefore, we plan to use classical molecular dynamics methods. Since there is no accurate force field to describe the interactions between elements Ge, S and Cu, we will use DFT calculations to generate a training set of high-level calculations and, optimize a reactive force field for large-scale classical MD.

3.2 Density functional theory

Density functional theory (DFT) is a powerful method to solve the many-body Schrödinger equation numerically. DFT is based on the idea that the ground-state energy of many electrons system can be expressed as a function of the density of electrons. The practical theory was introduced by Kohn and Hohenberg in the 60s [51]. The many-body Schrödinger equation under the approximations of N single-electron orbitals $|\Psi_I(\vec{r})\rangle$ can be expressed as:

$$\frac{-\hbar^2}{2m_e}\nabla^2\Psi_I(\vec{r}) + [U(\vec{r}) + \int d\vec{r}' \frac{e^2\rho(\vec{r}')}{|\vec{r}-\vec{r}'|} + \frac{\partial\varepsilon_{xc}[\rho]}{\partial n}]\Psi_I(\vec{r}) = \varepsilon_I\Psi_I(\vec{r}) \quad (3.1)$$

The first term on the left-hand side of Eq. 3.1 represents the kinetic energy of the electrons, the second and third terms are the ion-electron and electron-electron Coulomb energy and the last term is the exchange-correlation energy. Although the



exchange-correlation energy term is unknown, there are two common approximations to evaluate this term: the local density approximation and generalized gradient approximation.

3.2.1 Exchange-correlation potentials

The first approximation is called the “Local Density Approximation” (LDA). It is the simplest approximation and it can be expressed as:

$$\epsilon_{xc}[\rho] = \int \epsilon_{xc}[\rho(\vec{r})] \rho d\vec{r} \quad (3.2)$$

with $\epsilon_{xc}[\rho(\vec{r})]$ the exchange-correlation energy per particle of the homogeneous electron gas. The exchange energy can be computed as an analytical form $\epsilon_x[\rho] = -\frac{3}{4} \left(\frac{3\rho}{\pi}\right)^{\frac{1}{3}}$ [52] and the correlation energy can be calculated from Monte Carlo simulations [53]. The LDA is accurate to approximate systems with slowly varying density. Another common approximation is the “General Gradient Approximation” and can be expressed as [54]:

$$\epsilon_{xc}[\rho] = \int \epsilon_{xc}[\rho(\vec{r}), |\nabla\rho(\vec{r})|] \rho d\vec{r} = \int \epsilon_{xc}[\rho(\vec{r})] F_{xc}[\rho(\vec{r}), |\nabla\rho(\vec{r})|] \rho d\vec{r} \quad (3.3)$$

with $\epsilon_{xc}[\rho(\vec{r})]$ the exchange-correlation functional of the homogenous electron gas, F_{xc} is dimensionless and can be classified in three common forms which are: Becke (for example B88 developed in 1988) [55], Perdew and Wang (PW91) [56], and Perdew, Burke and Enzerhof (PBE) [57]. GGA is expected to improve results for less homogeneous systems and is a good approximation for structural optimization.



Although GGA is accurate for structural optimization, it often fails to describe the electronic properties of materials resulting in underestimated bandgaps. In 1993, Becke [58] developed the first hybrid exchange-correlation functional to improve various molecular properties. The idea of the hybrid functional is based on a combination of the local exchange and correlation functional (LDA or GGA) plus part of HF exact exchange functional. The most common Hybrid functional for crystals is HSE [59] and its form can be expressed as:

$$E_{xc}^{HSE} = aE_x^{HF,SR}(\omega) + (1 - a)E_x^{PBE,SR}(\omega) + E_x^{PBE,LR}(\omega) + E_c^{PBE} \quad (3.4)$$

The first term on the right-hand side represents the short-range HF exchange component, the second and third terms represent the short and long-range PBE exchange components. The final term represents the correlation component of the PBE functional. Hybrid functionals have further improvement in predicting the electronic and physical properties of materials compared to PBE. The most popular hybrid functional for molecular systems is B3LYP and the corresponding energy can be written as:

$$E_{xc}^{B3LYP} = E_x^{LDA} + a_0(E_x^{HF} - E_x^{LDA}) + a_x(E_x^{GGA} - E_x^{LDA}) + E_c^{LDA} + a_c(E_c^{GGA} - E_c^{LDA}) \quad (3.5)$$

3.2.2 A practical view of DFT

Nowadays, there are many ab initio programs based on DFT. For example: SIESTA



[60], ORCA [61], Vienna ab-initio simulation package (VASP) [62] and Quantum Espresso (QE) [63]. These codes allow calculating various important physical and electronic properties of crystals and molecules including band structure, the density of states, geometries, etc.

In this thesis, all DFT calculations are performed with VASP and ORCA. We choose VASP for calculating the physical properties of crystal and amorphous structure because it outperformed other software in speed and scalability. In addition, we prefer using ORCA for calculations of molecules because ORCA is free of charge software and it can accurately describe the interaction between atoms in molecules. VASP is based on pseudopotentials (PPs) and a plane wave basis set while ORCA is based on a linear combination of atomic basis set [64]. The concept of PPs is related to replacing the effect of the core electrons with an effective potential. PPs can accelerate dramatically the speed of the simulations. In addition, plane wave basis sets are more efficient because of the periodic nature of crystals. Self-consistent field iterations are performed to find the ground state density of the systems. If the free energy difference between ionic iterations is within expected tolerance, the DFT calculation converged and the ground state density of the system is obtained. Practically, we need to set the threshold values for stopping criteria for the electronic and ionic relaxations. The number of k-



points for DFT calculations is also important and determines how many points are used to sample the Brillouin zone usually described as an equally spaced mesh. One also need to decide on the kinetic energy cutoff to expand the plane wave basis set. All plane waves with a kinetic energy smaller than E_{cut} are included in the basis set as:

$$|G + K| < G_{cut} \text{ with } E_{cut} = \frac{\hbar^2 G_{cut}^2}{2m} \quad (3.6)$$

Using more k-points or a higher energy cutoff, will increase the accuracy of the calculation but also increase the computational cost. In ORCA, using larger basis sets will also increase the computational cost.

3.2.3 Molecular dynamics

Molecular dynamics (MD) is a simulation method for describing and predicting the motion of interacting many-body systems at the atomistic scale. MD is based on obtaining the force acting on atoms by taking partial derivatives of the potential energy with respect to the position of atoms [65]:

$$F_i(r_1, r_2, \dots, r_N) = -\nabla_{r_i} U(r_1, r_2, \dots, r_N) \quad (3.7)$$

with $U(r_1, r_2, \dots, r_N)$ the potential energy corresponding to the atomic positions. The position of the atoms at a later time $t+\Delta t$ can be predicted by numerically integrating Newton's equations. Various numerical integrators have been proposed including Verlet and velocity-Verlet [66]. The numerical integration or *timestep* has to be small enough



to include atomic vibrations, limiting the domain of MD to the microsecond timescales.

The potential energy U can be computed from first principle calculations (for example DFT) leading to *ab initio* MD or using empirical interatomic potentials (or force fields) at the basis of classical MD.

3.3 Classical molecular dynamics

Classical MD are atomistic simulations based on an empirical model called a “force field”. Force fields have various mathematical forms (and accuracy) and provide the energy (or forces) corresponding to an atomic configuration (i.e. the position and type of the atoms). Force fields are generated by mapping experimental data or first principle calculations. Practically, we use DFT to generate a training set of atomic environments and the force fields are derived by optimizing parameters of a mathematical model in order to describe at best the training or test data. Across the years, a hierarchy of empirical force fields have been proposed and we discuss the principal functional form below.

3.3.1 Traditional empirical interatomic potentials

There are two common pair potentials for MD: Morse [67] and Lennard-Jones [68] potentials. Morse potential is used to approximate the vibrational excitations of a chemical bond. Morse potential can be expressed as:

$$V_{ij} = D\{\exp[-2\alpha(r_{ij} - r_e)] - 2 \exp[-\alpha(r_{ij} - r_e)]\} \quad (3.8)$$

where r_{ij} and r_e are instantaneous and equilibrium distance between atoms i and j ,



D and α represent the strength of the chemical bond and possibility of the variations about equilibrium.

Lennard-Jones potential is used to describe weak interactions between neutral atoms and molecules. Lennard-Jones potential can be expressed as:

$$V_{ij} = 4\varepsilon \left[\left(\frac{\sigma}{r} \right)^{12} - \left(\frac{\sigma}{r} \right)^6 \right] \quad (3.9)$$

where ε represents the magnitude of the maximum depth of the potential well, σ represents the distance between the origin and equilibrium position and r represents the distance between neutral atoms or molecules. Pair potentials have limited transferability in a different environment of the atom. For instance, the parameters determined for molecules cannot be used to describe crystals.

In 1983, Daw and Baskes [69] developed the embedded atom method (EAM) for large-scale MD. The prediction using EAM for metals is more accurate than pair potentials due to the inclusion of electron density effects. The EAM model can be expressed as:

$$E_{total} = \sum_I G_I(\rho_{h,I}) + \frac{1}{2} \sum_{I,J} V_{IJ}(r_{IJ}) \quad (3.10)$$

The first term on the right-hand side represents the embedding energy depending on the local electron density which is a sum over the electron density at every atom. The second term on the right-hand side represents the pair potential energy depending on the distance between atoms I and J . EAM can solve the problem of limited transferability in a different environment of atoms because of the inclusion of the local



density which accounts for the dependence of the strength of individual bonds on the local environment.

In the early 90s, Goddard proposed a many-body functional force field [70]. The functional form of DREIDING can be expressed as:

$$V = V_b + V_\theta + V_\varphi + V_{vdw} + V_{elec} \quad (3.11)$$

The first three terms on the right-hand side represent bond stretching, bond bending and torsion respectively. These three terms correspond to bonded interactions. The two other terms represent van der Waals and electrostatic interactions. These two last terms correspond to non-bonded interactions. Bond stretching and bond bending potentials can be expressed as a simple harmonic function:

$$V_b (r_{IJ}) = \frac{k_b}{2} (r_{IJ} - r_0)^2 \quad (3.12)$$

$$V_\theta (\theta_{IJK}) = \frac{k_\theta}{2} (\theta_{IJK} - \theta_0)^2 \quad (3.13)$$

where r_0 and θ_0 represent the equilibrium bond length and bond angle, respectively.

In addition, the bond torsion potential term is related to every quartet of bonded atoms and can be expressed as:

$$V_\varphi (\varphi_{IJK}) = \frac{k_\varphi}{2} (1 + \cos 3\varphi_{IJK}) \quad (3.14)$$

The van der Waals and electrostatic terms in the DREIDING force field are expressed as Lennard-Jones and Coulomb. Although many-body potentials have been very successful to describe the large-scale molecular system, these potentials are limited to



fixed connectivity. Therefore, these potentials cannot describe chemical reactions between atoms. For instance, they cannot simulate ligand switching or change of coordination number. To overcome this limitation, reactive force fields have been proposed.

3.3.2 Reactive force fields

Reactive force fields such as Tersoff [71], ReaxFF [72] and COMB [73] are based on the notion of bond order (BO); an index describing the chemical environment of atoms during molecular dynamics simulations. The total energy includes many-body covalent interaction and non-bonding terms such as van der Waals and Coulomb forces. The total energy of the system can be express as [74]:

$$E_{system} = E_{bond} + E_{over} + E_{angle} + E_{tors} + E_{vdWaals} + E_{coulumb} \quad (3.15)$$

with E_{bond} the bond energy between atoms, E_{angles} and E_{tors} the three body valence angle strain and four body torsional angle strain, respectively. E_{over} is related to the energy penalty in case of over coordination of atoms, $E_{coulumb}$ and $E_{vdWaals}$ describe the electrostatic and dispersive non-bond interaction. In this thesis, we will focus on ReaxFF [72]. ReaxFF can be “trained” to describe the chemical systems from QM calculations or experimental data. Due to the evolving BO function during MD simulations, ReaxFF enables chemical reaction (formation and dissociation of bonds).



The environment-dependent charge distribution is critical for the proper determination of physical properties. ReaxFF has been originally coupled with the charge equilibration (QEq) developed by Goddard [75]. The QEq method is based on the minimization of the total electrostatic energy of the system expressed as:

$$E(\{R_i\}, \{q_i\}) = \sum_i \left(\chi_i^0 q_i + \frac{1}{2} H_i q_i^2 \right) + \sum_{i < j} q_i q_j J(R_{ij}) \quad (3.16)$$

where χ_i^0 and H_i represent the electronegativity and hardness of the atoms, respectively and, $J(R_{ij})$ the shielded (to avoid close range over-contributions) Coulomb function. Interatomic charges $\{q_i\}$ are calculated self-consistently, at every step of the simulation, based on the minimization of Eq. 3.16, assuming equilibrium of the chemical potentials $\left\{ \frac{\partial E}{\partial q_i} \right\}$ on each atom. ReaxFF has been successfully applied to model systems including metals [76], semiconductors [77], organic molecules [78] and interface [79]. ReaxFF is the efficient method of choice to simulate large systems including non-equilibrium chemical reaction such as the operation of emerging memory devices where the formation and dissolution of metallic filaments are critical.

Due to the expensive computational cost of FPMD simulations for large systems by using ORCA or VASP, we decide to perform high throughput classical MD simulations for investigating on physical properties and electronic properties of copper-doped germanium sulfide glasses at various compositions based on the ReaxFF implemented by LAMMPS. LAMMPS is a free classical MD code for atomistic modelling and it is



efficient for parallel computing by using spatial-decomposition approach to divide the simulation domain into small sub-domains and assigning to each core.



Chapter 4 Development of ReaxFF for Ge/S/Cu elements

4.1 Overview

Due to no current force field for describing the interaction between germanium sulfide glasses and copper, we developed the new reactive force field based on a training set of first principle calculations. In this section, we will introduce the method and procedure for developing and optimizing the reactive force field. We will first introduce the training set then, we will discuss the optimization algorithm and finally, we will perform validation tests with respect to recent literature.

4.2 Methodology and simulation details

4.2.1 Training set

In order to determine the parameters that describe the functional form of the interaction, the force field has to be optimized against a training set of electronic structure calculations. Figure 4.1 shows the diversity of training set for optimizing the ReaxFF including Ge, S and Cu.

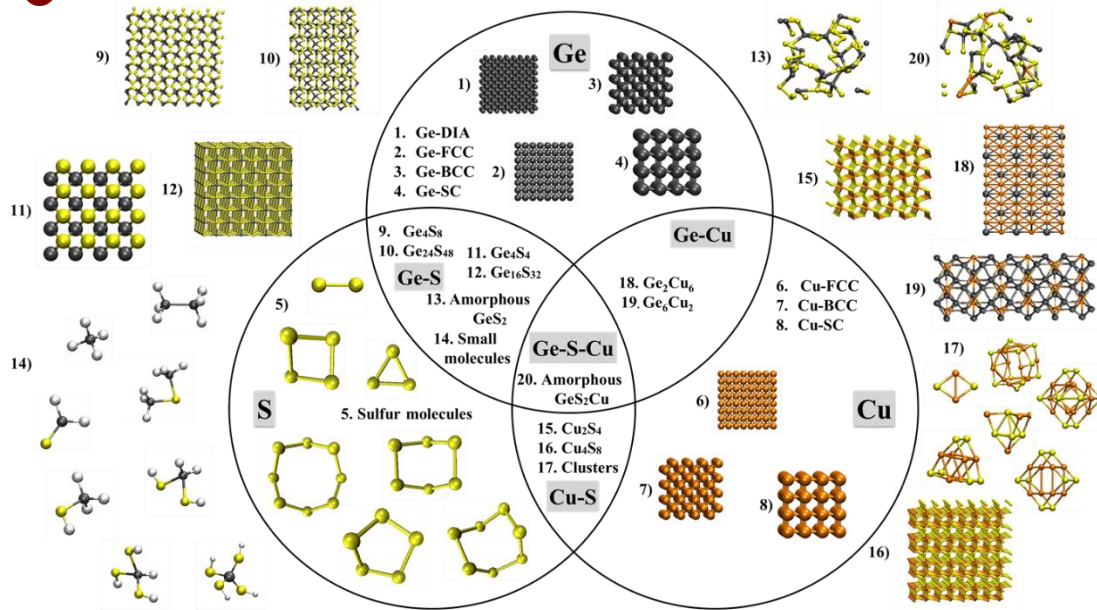


Figure 4.1. The training set for optimizing the ReaxFF including Ge, S and Cu

The training set for GeS/Cu includes EOS for crystals, dissociation curves of small molecules and a series of binding energy describing the relative stability of various amorphous structures including $\text{Ge}_{0.33}\text{S}_{0.67}$ and $\text{Ge}_{0.3}\text{S}_{0.61}\text{Cu}_{0.09}$. As it is often the case, we will use DFT calculations to generate the training set.

All DFT calculations for crystal structures have been performed with the VASP package [62] within the GGA approximation as proposed by PBE [57]. In addition, atomic structures have been relaxed until energies and forces reaching a tolerance of 10^{-4} eV and 10^{-1} eV/Å, respectively. The kinetic energy cutoff for the plane wave basis set is set to 500 eV and we integrated the k-mesh using a ratio of ≈ 40 k-mesh/lattice constant. EOS were performed by deforming the volume of the crystal cells isotropically between -15% to +15%. We use Grid-based Bader charge calculations to obtain the partial charge



distributions for every crystal structure and optimize Qeq parameters. The structure of small molecules was computed with DFT at the B3YLP level [80] and def2-TZVP basis set [64] as implemented in ORCA [61]. We computed potential energy surfaces including bond dissociation, angle bending and dihedral torsion for various molecules. In addition, we also included the enthalpy of formation of chemical reactions for reactions for different oxidation states of germanium and sulfur-contained molecules in order to train the over-coordination.

Amorphous structures of $\text{Ge}_{0.33}\text{S}_{0.66}$ (i.e. GeS_2) and $\text{Ge}_{0.3}\text{S}_{0.61}\text{Cu}_{0.09}$ were generated by a melt and quench method based on Born-Oppenheimer molecular dynamics as implemented in VASP. We used Γ point of the supercell to expand the wave functions with a kinetic energy cutoff of 400 eV. A timestep of 2 fs was selected to integrate the equations of motion and we use Nose-Hoover thermostat [81] to control electronic and ionic temperature. We initially assigned the 60 (20 Ge + 40 S) and 66 atoms (20 Ge + 40 S + 6 Cu) with a reasonable bond cutoff distance larger than 2.0 Å into the simple cubic unit cell with a density of 2.75 g/cm³. The structures are initially equilibrated at 2,000K in the canonical ensemble (NVT) for 15 ps. To train ReaxFF to describe various atomic environments, we generated 10 amorphous GeS_2 and 5 $\text{Ge}_{0.3}\text{S}_{0.61}\text{Cu}_{0.09}$ samples by restarting the calculation every 3 ps, for a total high temperature simulation of 42 ps. Then the liquid samples were quenched at 56.67K/ps to 300K, equilibrated at 300K for

10 ps and finally fully quenched to 0 K by performing relaxations for ions and cell.

4.2.2 Optimization algorithm

We used in-house optimizer written in Python to optimize the ReaxFF, the optimization method is based on Monte Carlo (MC) coupling with simulated annealing (SA) algorithm [82]. Figure 4.2 shows the procedures for optimizing the ReaxFF based on the algorithm.

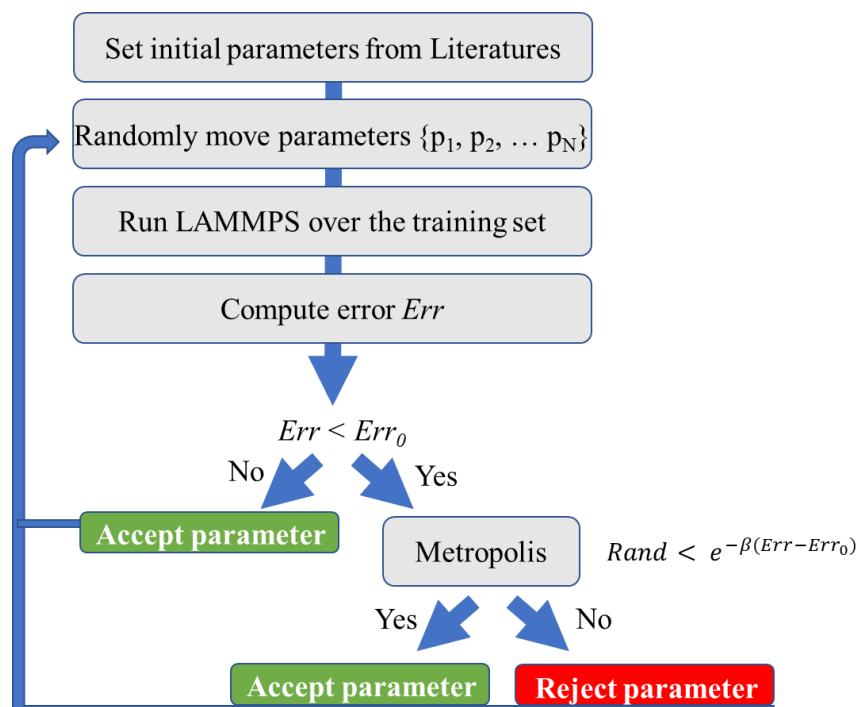


Figure 4.2. The procedures for optimizing the ReaxFF based on the algorithm

This algorithm previously used to developed parameters for MoTe₂/Cu [83]. At every step of the MC search, each parameter of the force field is randomly moved, and the error is calculated by the sum of the mean square errors between energies, forces, partial charges and cohesive energies computed with DFT and ReaxFF. The equation can be expressed as:



$$MSE = \sum_i^{N_{mol}} \frac{(P_i^{DFT} - P_i^{ReaxFF})^2}{N^2} \quad (4.1)$$

with P_i the parameter computed with DFT and ReaxFF and N a normalization factor.

The root mean square error is simply computed as $RMSE = \sqrt{MSE}$. The parameter move is accepted if the error of the current MC step (RMSE) is less than that of the previous step ($RMSE_0$). Additionally, a Metropolis criterion allows the random selection of some non-optimum parameters in order to expand the exploration space and avoid the force field function to be trapped in local minimum. Practically, if $\Delta Err = RMSE_0 - RMSE < 0$, we draw a random number (RAND) and the move is accepted if:

$$RAND < \exp(-\Delta Err/T) \quad (4.2)$$

with T a fictitious temperature. Moreover, we performed a simulated annealing (SA) to narrow down the acceptance ratio of the Metropolis criterion and to refine the optimization by lowering the temperature at every MC step. The SA is achieved by lowering T each times the whole series of parameters has been moved 10 times. Convergence is determined by the user once the ensemble of parameters is acceptable.

The initial parameters for the force field were taken from literature including Ge (and H) [84], S, Cu and their interactions Cu/S [85]. In addition, Ge/S and Ge/Cu were initialized from Si/O and Si/Cu [38]. The general parameters for Ge, S and Cu were fixed excepted the QEq parameters for Ge and S and we only modified S/S, Ge/S, S/Cu and Ge/Cu during the optimization. We first trained the QEq parameters for Ge/S based



on various crystal and amorphous phases of GeS and then other parameters were optimized by PES corresponding to various types of interaction in the training set.

4.2.3 Validation procedures

To validate the ability of optimized force field for describing the chemical interaction of germanium sulfide glasses at different compositions, we generated amorphous structures with the developed ReaxFF and compared their structural properties and electronic properties with recent literature including GeS₂ [21], GeS₃ and GeS₆ [25]. All validations for the developed force field have been performed by LAMMPS [86]. We generated the initial structures with the same method mentioned in section 4.2.1 of 192, 80 and 140 atoms for GeS₂, GeS₃ and GeS₆ respectively. A 0.5 fs timestep was used for integrating the equation of motion. Simulations were performed in the isobaric-isothermal ensemble (NPT) with a Nose-Hoover thermostat. The GeS₂, GeS₃ GeS₆ systems were thermalized at 1500K, 1200K and 800K for 100 ps. In order to perform the statistical analysis, we selected 5 liquid samples by restarting the calculation every 10 ps, the total process for melting takes 140 ps. All samples were quenched to 300K with a slow cooling rate of 10K/ps. The amorphous structures were equilibrated at 300K for 100ps. The final 50 ps simulations at same temperature were performed in the isovolumetric-isothermal ensemble (NVT) with a Nose-Hoover thermostat for



structural analysis. In addition, amorphous structures have been relaxed after 100ps thermalization for evaluating the averaged density by performing relaxations for the cell and ionic positions, respectively. Similarly, we generated Cu doped amorphous germanium sulfides structures corresponding to compositions GeS_3 and GeS_6 with 5%, 20%, 25%, 35% and 50% content of copper respectively. The melting temperature was adjusted to prevent the system to vaporize.

4.2.4 Structural analysis

The amorphous structures were characterized by computing the RDF and total structure factor [87]. Total structure factor characterized the medium range ordering of amorphous structure by the first sharp diffraction peak (FSDP) and it was calculated by performing Fourier transform for the total RDF. In addition, coordination analysis was performed with the R.I.N.G.S software [88]. The coordination number is defined as the count for the existence of a bond between two atoms i of species α and j of species β determined by the bond cutoff distance. The bond cutoff distance for Ge-Ge, Ge-S, S-S, Cu-Cu, Cu-Ge and Cu-S were taken as 2.68, 2.86, 2.58, 3.0, 3.0 and 3.0 Å.

4.3 Results and discussion

4.3.1 Force field optimization

4.3.1.1 Amorphous structures

Here, we show that the QEq parameters in ReaxFF have been optimized with Bader charge in amorphous samples and 4 germanium sulfide crystals based on the DFT



calculations. The mean absolute errors between QEq and Bader charge of 10 amorphous $\text{Ge}_{0.33}\text{S}_{0.67}$ and 5 $\text{Ge}_{0.3}\text{S}_{0.61}\text{Cu}_{0.09}$ samples were shown in table 4.1.

Table 4.1. Comparison of mean absolute error for charge (e/atom) by computing with DFT and ReaxFF for different amorphous structures.

Amorphous samples	Mean absolute error δQ
$\text{aGe}_{0.33}\text{S}_{0.67}$ (1)	0.09
$\text{aGe}_{0.33}\text{S}_{0.67}$ (2)	0.08
$\text{aGe}_{0.33}\text{S}_{0.67}$ (3)	0.07
$\text{aGe}_{0.33}\text{S}_{0.67}$ (4)	0.09
$\text{aGe}_{0.33}\text{S}_{0.67}$ (5)	0.08
$\text{aGe}_{0.33}\text{S}_{0.67}$ (6)	0.08
$\text{aGe}_{0.33}\text{S}_{0.67}$ (7)	0.07
$\text{aGe}_{0.33}\text{S}_{0.67}$ (8)	0.08
$\text{aGe}_{0.33}\text{S}_{0.67}$ (9)	0.07
$\text{aGe}_{0.33}\text{S}_{0.67}$ (10)	0.08
$\text{aGe}_{0.30}\text{S}_{0.61}\text{Cu}_{0.09}$ (1)	0.1
$\text{aGe}_{0.30}\text{S}_{0.61}\text{Cu}_{0.09}$ (2)	0.09
$\text{aGe}_{0.30}\text{S}_{0.61}\text{Cu}_{0.09}$ (3)	0.1
$\text{aGe}_{0.30}\text{S}_{0.61}\text{Cu}_{0.09}$ (5)	0.09
$\text{aGe}_{0.30}\text{S}_{0.61}\text{Cu}_{0.09}$ (5)	0.1

We found very low mean absolute error for amorphous structures between QEq and Bader charges were less than or equal 0.1e per atom for each amorphous structure in the training set. In addition, the optimized values of 2.35 eV and 8.00 eV for the electronegativity of Ge and S were consistent with oxygen and silicon reported in ReaxFF_SiO of 2.41 and 8.00 eV respectively and corresponding to slightly less electronegative elements. Remarkably, these QEq parameters were able to transfer to



the amorphous Ge/S/Cu structures, not included in the training set. The original QEq parameters for Cu were able to describe with accurate charges on Ge/Cu crystals as well as on key amorphous $\text{Ge}_{0.3}\text{S}_{0.61}\text{Cu}_{0.09}$, part of the target of the targeted ternary diagram.

4.3.1.2 Small molecules

We compared potential energy surfaces including bond dissociation, angle bending and dihedral torsion for various molecules by DFT and the optimized force field reported in figure 4.3. The molecule name was mentioned in the title of each subplot and the location of the bond (angle/dihedral) dissociated (bent/twisted) was indicated as the dash and equal symbols representing a single and double bond, respectively.

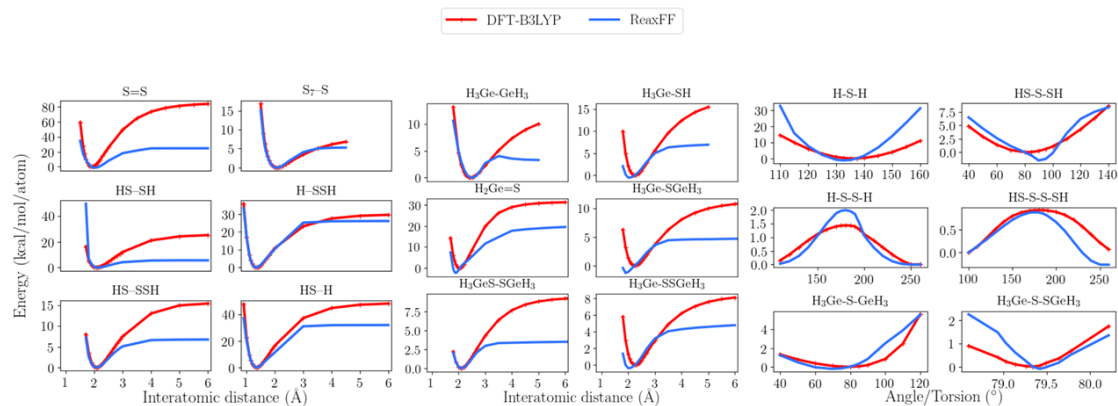


Figure 4.3. (a) The relation between energy and interatomic distance during bond dissociation of $\text{S}=\text{S}$, $\text{S}-\text{S}$, $\text{S}-\text{H}$, (b) $\text{Ge}-\text{Ge}$, $\text{Ge}-\text{S}$ and $\text{Ge}=\text{S}$ bond (c) relation between energy and various angle bending/dihedral angle torsion of some small molecules included in the training set computed with optimized ReaxFF (blue) and DFT (red).

We found that the force field is able to predict the similar potential energy surface near equilibrium positions with DFT including the equilibrium position. However, the bond



dissociation energies were often underestimated as shown in Fig 4.1 (a) and (b). We compared the energetics and the cohesive energy of some small sulfur cycles compared to DFT also included in the training set and were reported in table 4.2.

Table 4.2. Cohesive energy corresponding to reactions with over-coordinated S atoms as well as some small cyclic sulfur cluster. All the units for energies were reported in kcal/mol/atom of the reactant.

Chemical reaction	DFT	ReaxFF
$(\text{SH})_2\text{-S-(SH)}_2 \rightarrow \text{HS-S-SH} + \text{HS-SH}$	25.39	24,41
$(\text{HS})_2\text{-S-S-(SH)}_2 \rightarrow \text{HS-S-S-SH} + \text{HS-SH}$	9.99	9.21
$\text{S}_3 \rightarrow 3/2(\text{S}_2)$	-9.07	-9.98
$\text{S}_4 \rightarrow 4/2(\text{S}_2)$	-8.68	-9.85
$\text{S}_5 \rightarrow 5/2(\text{S}_2)$	-14.39	-17.19
$\text{S}_6 \rightarrow 6/2(\text{S}_2)$	-16.21	-17.16
$\text{S}_7 \rightarrow 7/2(\text{S}_2)$	-17.06	-19.1
$\text{S}_8 \rightarrow 8/2(\text{S}_2)$	-19.7	-20.73
$(\text{H}_3\text{Ge})_2\text{-S-S-(GeH}_3)_2 \rightarrow 2 \times \text{H}_3\text{Ge-S-GeH}_3$	6.38	4.48
$(\text{H}_3\text{Ge})_2\text{-S-S-(GeH}_3)_2 \rightarrow \text{H}_3\text{Ge-S-GeH}_3 + \text{H}_3\text{Ge-GeH}_3$	1.96	0.74
$(\text{H}_3\text{Ge})(\text{HS})\text{-S-S-(SH)(GeH}_3) \rightarrow \text{H}_3\text{Ge-S-S-GeH}_3 + \text{HS-SH}$	7.76	4.49

4.3.1.3 Crystals

In addition to the small molecules, the cohesive energy of the crystal structure was also included in the training set. The label of crystal structures was defined as the number of atoms in the conventional cell. We selected three crystal phases of germanium disulfide with similar formation energy determined by DFT calculation at the PBE level including Ge_4S_8 , $\text{Ge}_{24}\text{S}_{48}$ and the layered ground state structure $\text{Ge}_{16}\text{S}_{32}$. The puckered monochalcogenide Ge_4S_4 structure was also included in the training set for optimizing Ge/S parameters. These structures covered the coordination for germanium sulfides



corresponding to three (III) and four-fold (IV) coordination for Ge and, two (II) and three-fold (III) coordination for S. Crystals of Cu_2S_4 , Cu_4S_8 , Cu_2S_6 and Cu_2Ge_6 and Cu_6Ge_2 were taken from the Material Project database [89] in order to optimize S/Cu and Ge/Cu parameters. We also selected additional simple crystal phases of Copper and ternary Cu_2GeS_3 and Ge_2GeS_4 taken from the database to demonstrate the transferability of the optimized parameters. The cohesive energy of various crystal structures computed with DFT and the optimized ReaxFF are reported in Table 4.3.

Table 4.3. Cohesive energy (kcal/mol/atom) for unary crystals and, formation energy (kcal/mol/atom) for binary and ternary crystals, mean absolute error for energy (kcal/mol/atom) and charges (e/atom) based on the DFT optimized structure computed with DFT and ReaxFF for various crystals. Materials project IDs and the nearest neighbour partial coordination were also provided. Additional data were included to demonstrate the transferability of the optimized parameters.

	Cohesive energy		Mean absolute error		ID	Coordination
	DFT	ReaxFF	δE	δQ		
Ge-DIA	-102.16	-90.3	4.15			IV
Cu-FCC	-80.7	-81.2	3.53			XII
Cu-BCC	-79.8	-79.51	1.78			VIII
Cu-SC	-69.9	-67.24	4.01			VI
$\text{Ge}_{16}\text{S}_{32}$	-20.4	-20.97	2.09	0.05	mp-572892	IV/II
$\text{Ge}_{24}\text{S}_{48}$	-20.25	-20.95	0.79	0.03	mp-542613	IV/II
Ge_4S_8	-19.92	-21.32	0.52	0.05	mp-7582	IV/II
Ge_4S_4	-15.49	-6.51	0.4	0.03	mp-2242	III/III
Cu_2S_4	-15.1	-13.46	9.36	0.29	mp-849086	VI/VI
Cu_4S_8	-15.49	-6.51	10.28	0.30	mp-1068	VI/VI
Cu_2Ge_6	7.00	7.00	10.68	0.05	mp-1025440	III/III
Cu_6Ge_2	-0.12	-0.12	4.21	0.07	mp-19724	Multiple
Cu_2GeS_3	-17.01	-11.75	2.44	0.4	mp-1072589	IV/IV/IV
Cu_2GeS_3	-15.46	-9.55	2.12	0.3	Mvc-13350	IV/IV/III



We used the original Ge/Ge and Cu/Cu parameters for the ReaxFF and showed the cohesive energy of Ge-diamond was slightly higher than the DFT results while the cohesive energy of Cu crystals was nearly equivalent to DFT values. In addition, the force field always predicts lower cohesive energy in germanium disulfide crystals and higher cohesive energy in monosulfide Ge_4S_4 . However, the force field is not able to predict the same ground state structure as DFT based on PBE functional and represented a challenge to resolve with an empirical interatomic potential. Formation energies of the copper disulfide and copper germanium crystal phase agree well with DFT results.

Figure 4.4. shows the EOS for the crystal structures computed with DFT and the optimized force field by isotropic deformations.

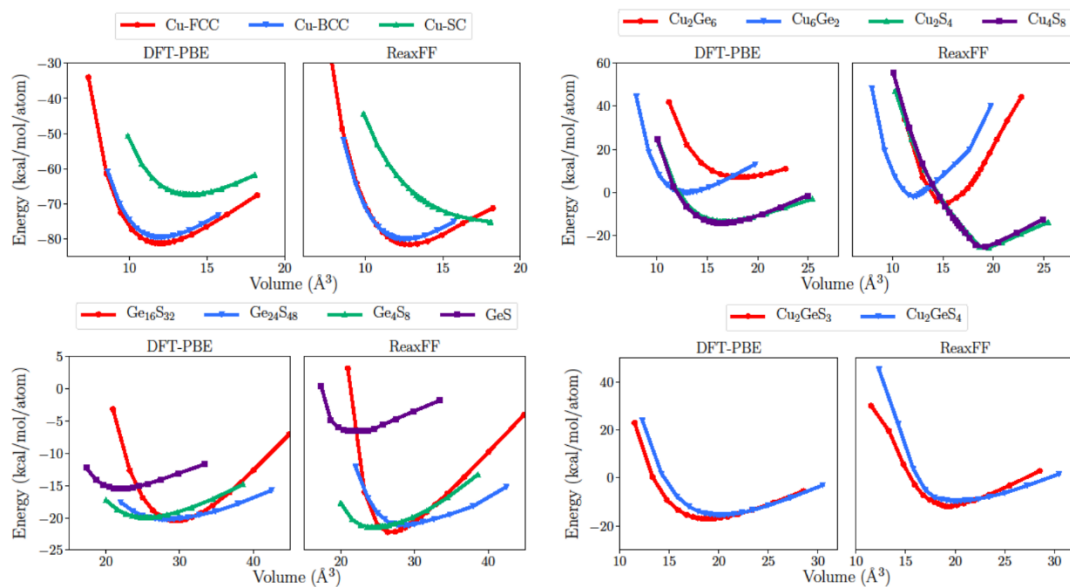


Figure 4.4. Energy curve for the EOS of the (a) various crystal phases of Cu, (b) crystals GeS and GeS_2 , (c) CuGe_3 , Cu_3Ge and CuS_2 , (d) Cu_2GeS_3 and Cu_2GeS_4 with isotropic deformation. The minimum energy of EOS is shifted to their corresponding cohesive/formation energy.



The force field is able to reproduce the equilibrium volume and corresponding energies with DFT excepted copper disulfides and Cu_2Ge_6 due to the fix general parameters for Ge and Cu in the training set through the optimization.

4.3.1.4 Clusters

Furthermore, we added the formation energy of some small CuS clusters in the training set to optimize the Cu/S parameters. We compared the cohesive energy of small CuS clusters computed with DFT and ReaxFF were reported in table 4.3 and the ground state structures are taken as the Cu_2 and S_2 molecules.

Table 4.4. Cohesive energy of small CuS clusters computed with DFT and the optimized ReaxFF (in kcal/mol/atom).

Name	DFT	ReaxFF
Cu_2S_2	-15.56	-16.18
Cu_4S_4	-26.34	-29.01
Cu_6S_6	-31.33	-31.52
Cu_8S_8	-32.49	-28.12
$\text{Cu}_{10}\text{S}_{10}$	-30.67	-27.44
$\text{Cu}_{12}\text{S}_{12}$	-29.62	-27.08

We found that the optimized force field predicted Cu_6S_6 to be ground state while PBE predicted Cu_8S_8 to be ground state.

4.3.2 Validations

4.3.2.1 Germanium sulfide glasses

One of the main requirements of a reliable force field was to be able to describe the glassy germanium sulfides. In order to validate our work. We generated an ensemble of



amorphous GeS_x ($x=2,3$ and 6) structures and compared the physical properties of the structures with recent literature including experimental findings and simulation results.

The comparison of the averaged atomic density of 5 amorphous GeS_2 samples generated by the optimized ReaxFF with experimental findings was shown in Table 4.5.

Table 4.5. The mean and standard deviation of the calculated atomic density for amorphous GeS_2 .

Amorphous GeS_2	Ref. [90]	DFT-PBE	ReaxFF
Density(g/cm^3)	2.7-2.8	2.73 ± 0.02	2.75 ± 0.09

The results are in good agreement with experimental findings. Remarkably, the calculated atomic density of GeS_2 by ReaxFF is close to our DFT results with 10 amorphous samples corresponding to $2.73 \pm 0.02 \text{ g}/\text{cm}^3$. We compared the total radial distribution function and partial radial distribution function of amorphous GeS_2 averaged over 10 and 5 samples by DFT and the optimized ReaxFF with FPMD [21] as shown in figure 4.5.

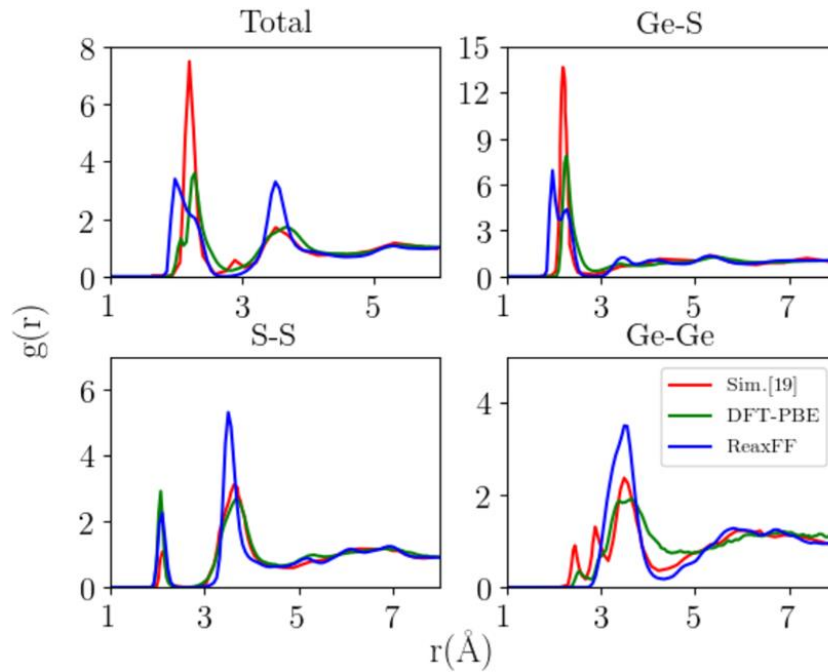


Figure 4.5. Comparison between total and partial radial distribution functions of amorphous GeS_2 averaged over 10 and 5 samples computed by DFT, the optimized ReaxFF with FPMD [21].

The optimized force field is able to reproduce all the FPMD features including a number of relevant peaks and their position excepted partial Ge-Ge and total radial RDF. The first and second peak of the partial Ge-Ge RDF generated by ReaxFF are disappeared due to a very low fraction of homopolar bond between Ge-Ge and edge-sharing tetrahedra corresponding to the first and second peak compared with ref [23]. In addition, the first peak of total RDF for the optimized force field at 2.0 Å is attributed by the underestimation of Ge-S bond length as shown in figure 4.1. (b).

We also compared the total structure factor averaged over 10 and 5 samples by DFT and ReaxFF with the FPMD [21] in figure 4.6.

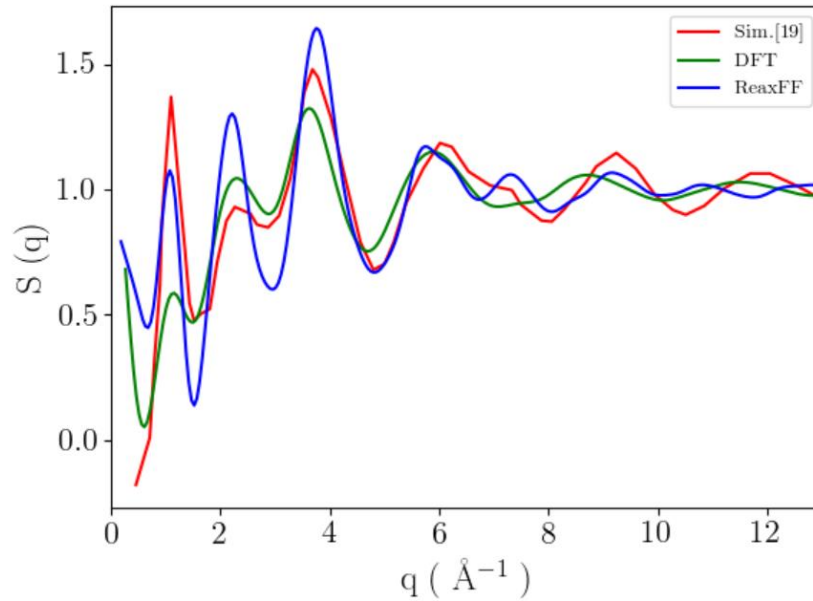


Figure 4.6. Comparison of total structure factor of amorphous GeS_2 averaged over 10 and 5 samples computed by DFT, the optimized ReaxFF with FPMD [21].

Both simulation results are able to predict the number of peaks and their location compared with FPMD. Interestingly, the ReaxFF describes the first sharp diffraction peak better than DFT results. We performed the defect analysis averaged over 10 and 5 samples by the DFT and the ReaxFF and compared with FPMD as shown in figure 4.7.

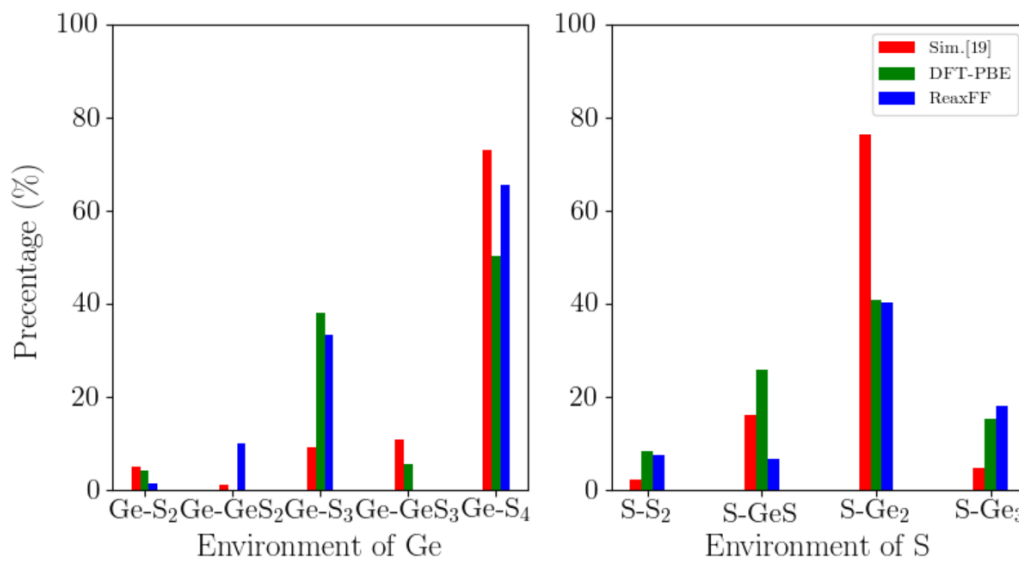


Figure 4.7. Comparison of defect distributions of amorphous GeS_2 averaged over 10 and 5 samples computed by DFT, the optimized ReaxFF with FPMD [21].



From the amorphous structures generated by the ReaxFF, we found approximately that 65.5% of Ge atoms are four-fold coordinated to S atoms and 40% of S atoms are two-fold coordinated to Ge atoms. However, this is less compared to Ref. [15] showing 73% and 76%, respectively and it can be explained by the overprediction the number of defects for the CGs systems based on PBE functional. Car-Parrinello MD based on the hybrid functional are common for modelling of the CGs systems due to the accurate description of defect distribution compared to the experimental findings [9]. The force field can be improved by adding amorphous structure generated by Car-Parrinello MD into the training set. In addition to validating with amorphous GeS₂, the structural properties of GeS₃ and GeS₆ were also investigated. Table 4.6 shows the comparison of the averaged atomic density of 5 amorphous GeS₂ samples generated by the optimized ReaxFF with experimental findings [90].

Table 4.6. The mean and standard deviation of the atomic density for amorphous GeS₃ and GeS₆.

Density(g/cm ³)	Ref. [90]	ReaxFF
GeS ₃	2.5-2.7	2.43±0.08
GeS ₆	2.3-2.4	2.20±0.09

the averaged density of amorphous GeS₃ and GeS₆ by ReaxFF are little lower than experimental finding. Figure 4.8 shows the comparisons of total radial distribution function and partial radial distribution function in amorphous GeS₃ and GeS₆ generated by ReaxFF with FPMD [25]

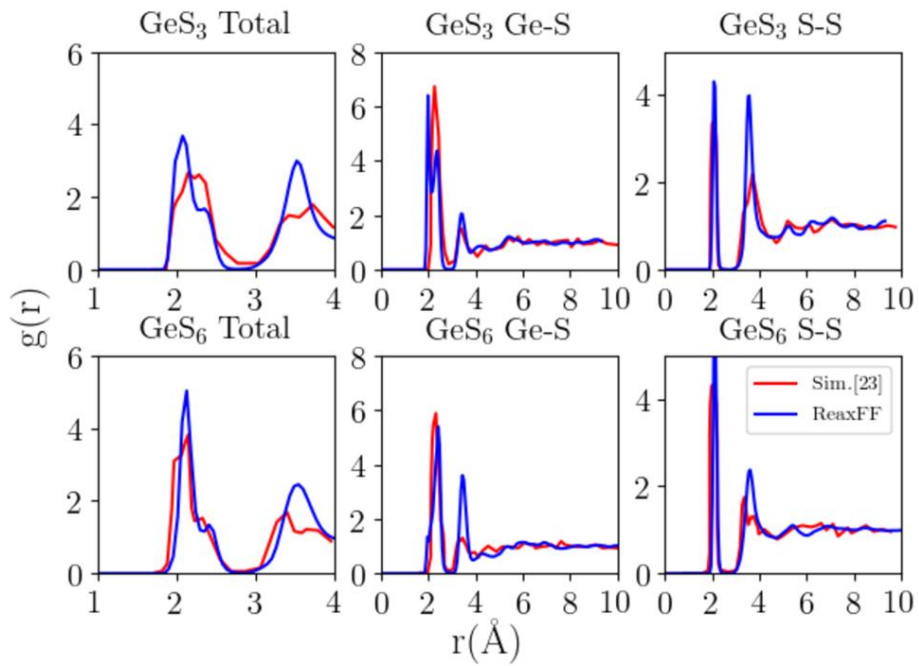


Figure 4.8. Total and partial RDF of amorphous GeS_3 and GeS_6 averaged over 5 samples computed by ReaxFF and FPMD [25].

The ReaxFF can reproduce all the number of relevant peaks and their positions.

However, the splitting of two peaks in partial Ge-S distribution can be explained by the

underestimation of Ge-S bond length as shown in figure 4.1. (b). We compared the

coordination number of Ge-S in GeS_3 and GeS_6 glasses with FPMD [25] in figure 4.9.

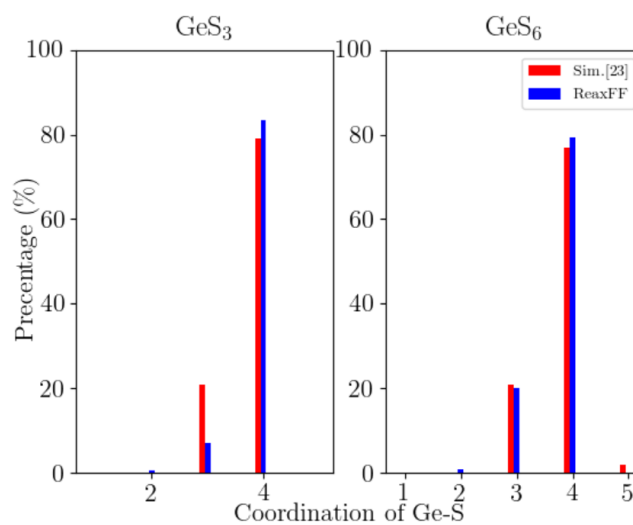


Figure 4.9. The coordination number of Ge-S in glassy GeS_3 and GeS_6 averaged over 5 samples generated by the ReaxFF and FPMD [25].



We found approximately that 80% and 83% of Ge atoms are four-fold coordinated to S atoms. Interestingly, this is little more compared to FPMD results showing 78% and 80% and it shows that the force fields describing the coordination number of Ge in the sulfur-rich Ge-S binary glassy system are comparable to FPMD results.

4.3.2.2 Copper doped germanium sulfide glasses

Figure 4.10. shows the atomic density of $(\text{GeS}_3)_{1-x}\text{Cu}_x$ and $(\text{GeS}_6)_{1-x}\text{Cu}_x$ with $x = 0.05, 0.2, 0.25, 0.35$ and 0.5 averaged over 5 samples by ReaxFF and FPMD

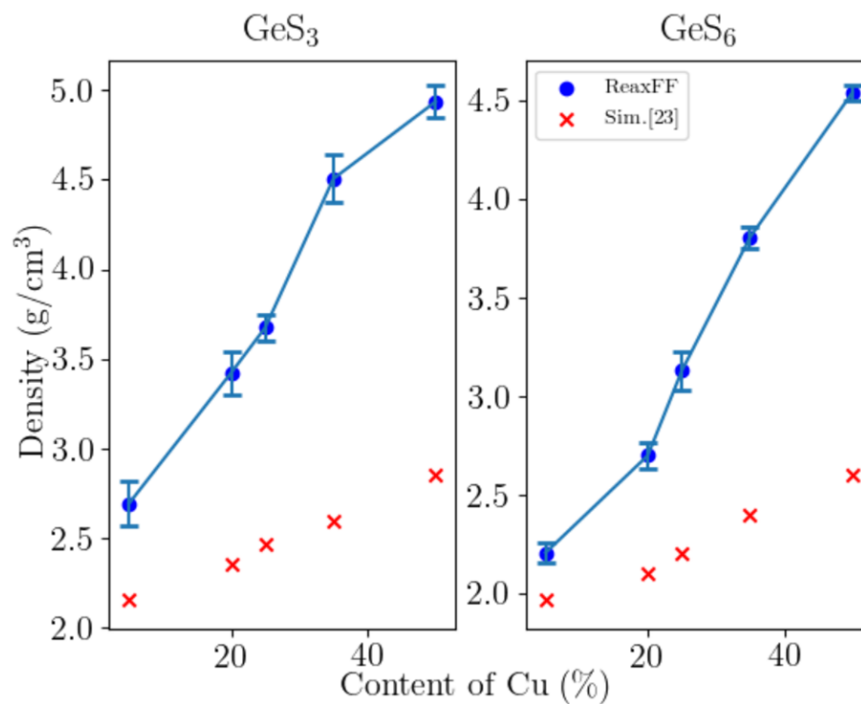


Figure 4.10. the averaged atomic density of $(\text{GeS}_3)_{1-x}\text{Cu}_x$ and $(\text{GeS}_6)_{1-x}\text{Cu}_x$ with $x = 5\%, 20\%, 25\%, 35\%$ and 50% generated by ReaxFF and FPMD [25].

We found the calculated atomic density of copper doped GeS_3 and GeS_6 are much higher than FPMD results at various Cu concentration. However, the increasing trend of



atomic density is consistent with silver-doped germanium sulfur glasses mentioned in previous experimental findings [31]. We compared the total RDF of amorphous $(\text{GeS}_3)_{1-x}\text{Cu}_x$ and $(\text{GeS}_6)_{1-x}\text{Cu}_x$ with $x = 0.05$ and 0.2 averaged over 5 samples computed by ReaxFF with FPMD [25] as shown in figure 4.11.

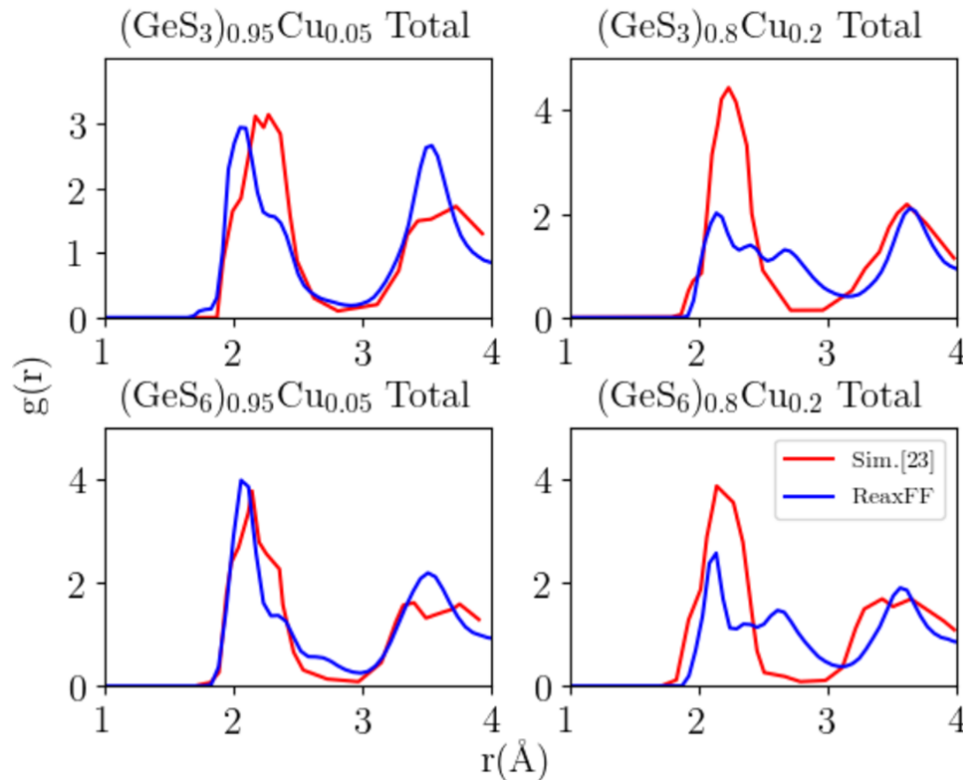


Figure 4.11. The averaged total RDF of $(\text{GeS}_3)_{1-x}\text{Cu}_x$ and $(\text{GeS}_6)_{1-x}\text{Cu}_x$ with $x = 5\%$, 20% generated by ReaxFF and FPMD [25].

We found that the ReaxFF generally are able to predict the number of peaks and position for glassy $(\text{GeS}_3)_{0.95}\text{Cu}_{0.05}$ and $(\text{GeS}_6)_{0.95}\text{Cu}_{0.05}$ systems with FPMD results. However, the splitting of the first peak for $(\text{GeS}_3)_{0.95}\text{Cu}_{0.2}$ and $(\text{GeS}_6)_{0.95}\text{Cu}_{0.2}$ systems leading three distribution including Ge-S bond distance around 2.0 and 2.3 \AA as well as Cu-S and Cu-Cu bond distance around 2.8 \AA .



The figure 4.12 shows the comparison of the coordination number of Ge-S for amorphous $(\text{GeS}_3)_{1-x}\text{Cu}_x$ and $(\text{GeS}_6)_{1-x}\text{Cu}_x$ systems at 0.05 and 0.2 Cu concentration with FPMD [25].

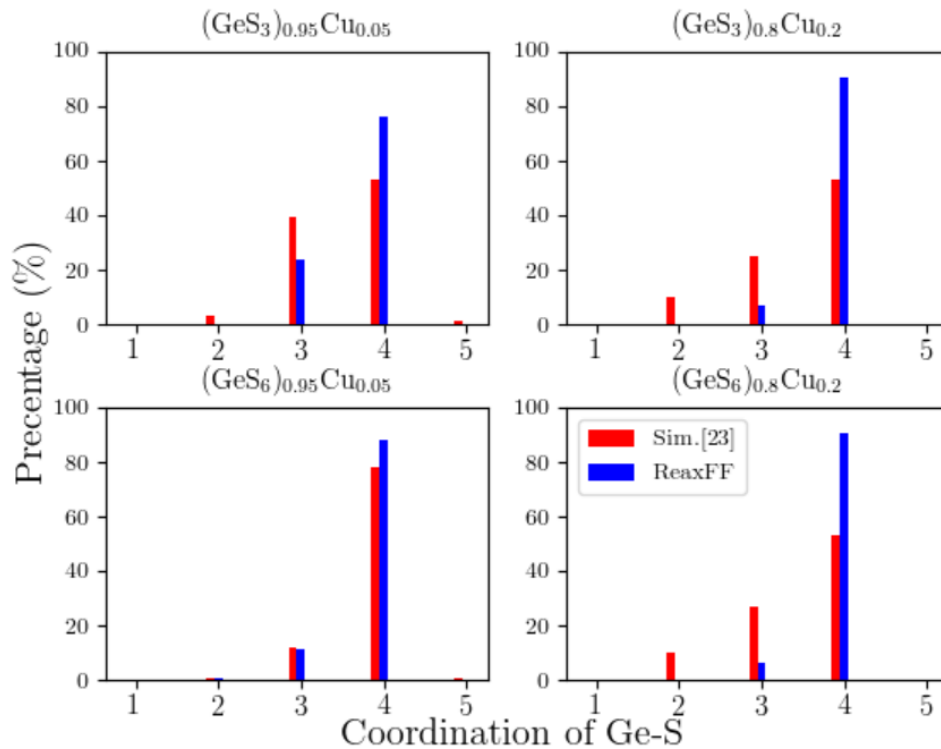


Figure 4.12. Coordination of Ge-S for $(\text{GeS}_3)_{1-x}\text{Cu}_x$ and $(\text{GeS}_6)_{1-x}\text{Cu}_x$ systems with $x = 5\%$ and 20% and FPMD [25].

We found that the ReaxFF always overpredict the number of Ge atoms with four-fold coordinated to S atoms for all compositions compared with FPMD. The calculated percentage of 4-fold coordination for all compositions are around 80% and similar to the undoped glassy GeS_3 and GeS_6 systems. It can be explained by the ReaxFF always overestimate of Ge-Cu bond distance. Figure.4.13 shows the temperature-dependent diffusion coefficient of Cu and corresponding activation energy for Cu diffusing in glassy $(\text{GeS}_3)_x\text{Cu}_{1-x}$ and $(\text{GeS}_6)_x\text{Cu}_{1-x}$ with $x = 5\%$ and 20% generated by ReaxFF.

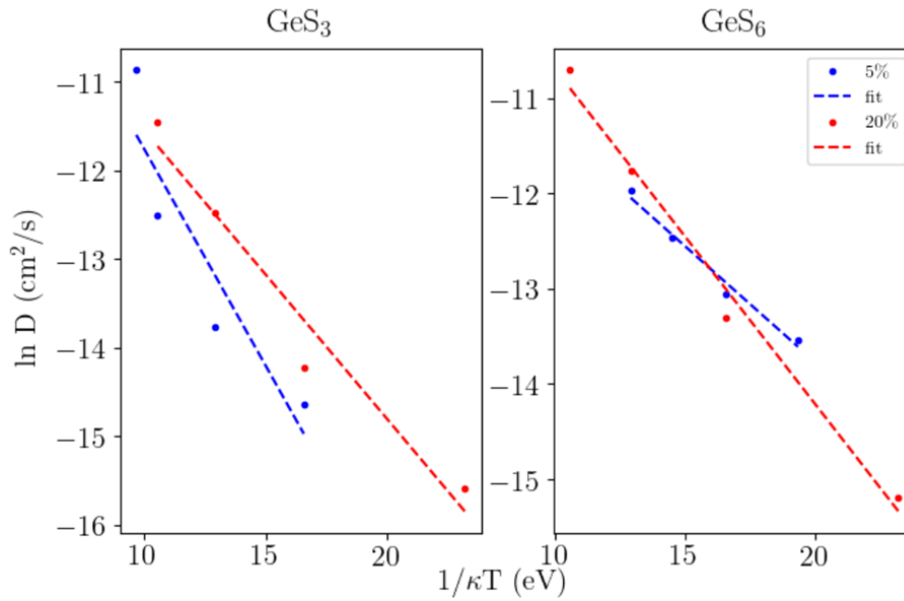


Figure 4.13. Temperature-dependent diffusion coefficients of Cu in (left) GeS_3 and (Middle) GeS_6 with 5% and 20% content of Cu generated by ReaxFF.

We found that the ReaxFF is able to predict the similar activation energy within 0.1 eV energy difference compared with FPMD [25] excepted $(\text{GeS}_3)_{0.95}\text{Cu}_{0.05}$ as shown in table 4.7 due to the temperature-dependent diffusion coefficients at 1300K closed to the melting point leading overestimation of linear fit for evaluating activation energy

Table 4.7. Activation energy of copper diffusion in GeS_3 and GeS_6 with 5% and 20% content of Cu by FPMD [25]) and ReaxFF.

Compositions	FPMD [25]		ReaxFF	
	5%	20%	5%	20%
GeS_3 (in eV)	0.27	0.25	0.49	0.33
GeS_6 (in eV)	0.27	0.3	0.24	0.35

The activation energy for $(\text{GeS}_3)_{0.95}\text{Cu}_{0.05}$ can be reduced for 0.49 to 0.34 eV and if we use other three diffusion coefficients to perform linear fitting. It shows that the ReaxFF is able to evaluate the reliable activation energy of Cu diffusion in the germanium sulfide glasses at various compositions.



Chapter 5 Exploring the compositions of $\text{Ge}_x\text{S}_y\text{Cu}_z$ for resistance switching

5.1 Overview

Our final goal is to find the compositions for ultra-fast resistance switching devices.

The diffusivity of Cu in the glass matrix plays a vital role in the performance of resistance switching including switching time and operation power. In this chapter, we performed high throughput calculations to investigate the dynamical properties and electronic properties for copper-doped germanium sulfide glasses at various compositions. Due to the large compositions and size of systems, it is computationally expensive to generate amorphous structures from scratch with DFT. Therefore, we will use the newly developed ReaxFF to generate amorphous structures and use DFT to study the electronic properties.

5.2 Stimulation details

All MD calculations have been performed with LAMMPS. Two sets of amorphous structures of $\text{Ge}_x\text{S}_y\text{Cu}_z$ ($X+Y+Z = 1$) were generated containing 540 and 60 atoms following a melt-and-quench procedure similar to the simulation detail Chapter 4 Section 4.2.3. We varied the content of Ge, S and Cu between 0.1 to 0.8 with steps of 0.1 for a total of 36 amorphous structures. We use a cooling rate of 10K/ps and simulations were performed in the NPT ensemble. The activation energy of Cu was extracted by computing its corresponding MSD at various temperatures for 1 ns in the



range 500-2000 K. Figure 5.1. shows the quenching procedure (step 1) and, the calculation of the activation energy for each composition (step 2).

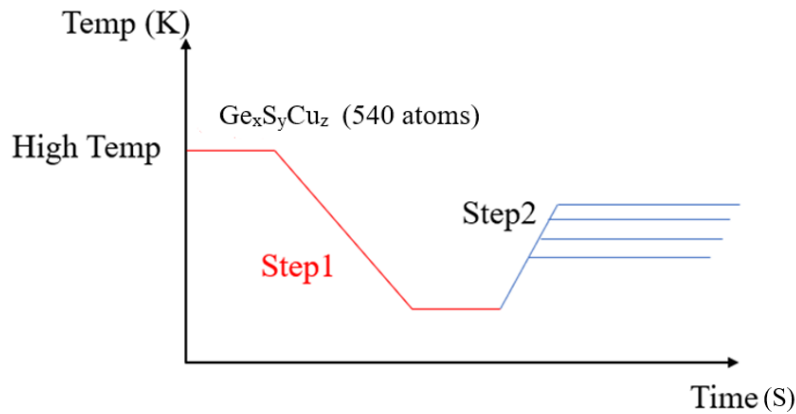


Figure 5.1. The procedures for calculating activation energy for Cu diffusion in the copper-doped germanium glasses at various compositions.

To evaluate the atomic structures, we performed defect analysis of the fully relaxed composition with the lowest activation energy at high and low Cu content. Bond cutoff distances for Cu-Ge, Cu-S and Cu-S were taken as 3.0 Å. DFT calculations were performed on the small cell to relax the lattice constant and ionic position until reaching the threshold of 10^{-4} eV and 0.1 eV/Å based on the conjugate gradient method implemented by VASP. We perform single step self-consistent field calculation for investigating the electronic density of state of copper-doped chalcogenide glasses at various compositions based on PBE functional. The kinetic energy cutoff for the plane wave basis set is set to 500 eV and we integrated the k-mesh using $2 \times 2 \times 2$. In addition, we selected three compositions with a fixed ratio of Ge and S atoms at the various content of Cu for further analysis.

To evaluate the normalized cluster size of Cu in the amorphous structures we performed distance based cluster analysis over the Cu atoms for the relaxed structures with a cutoff of 2.8 Å. The normalized cluster size can be expressed as the number of Cu atoms in the largest cluster divided by a total number of Cu atoms in the structure.

5.3 Results and discussions

5.3.1 Activation energy

Figure 5.2. shows the magnitude of the activation energy of Cu diffusing in germanium sulfide glasses at various compositions in a form of a ternary diagram.

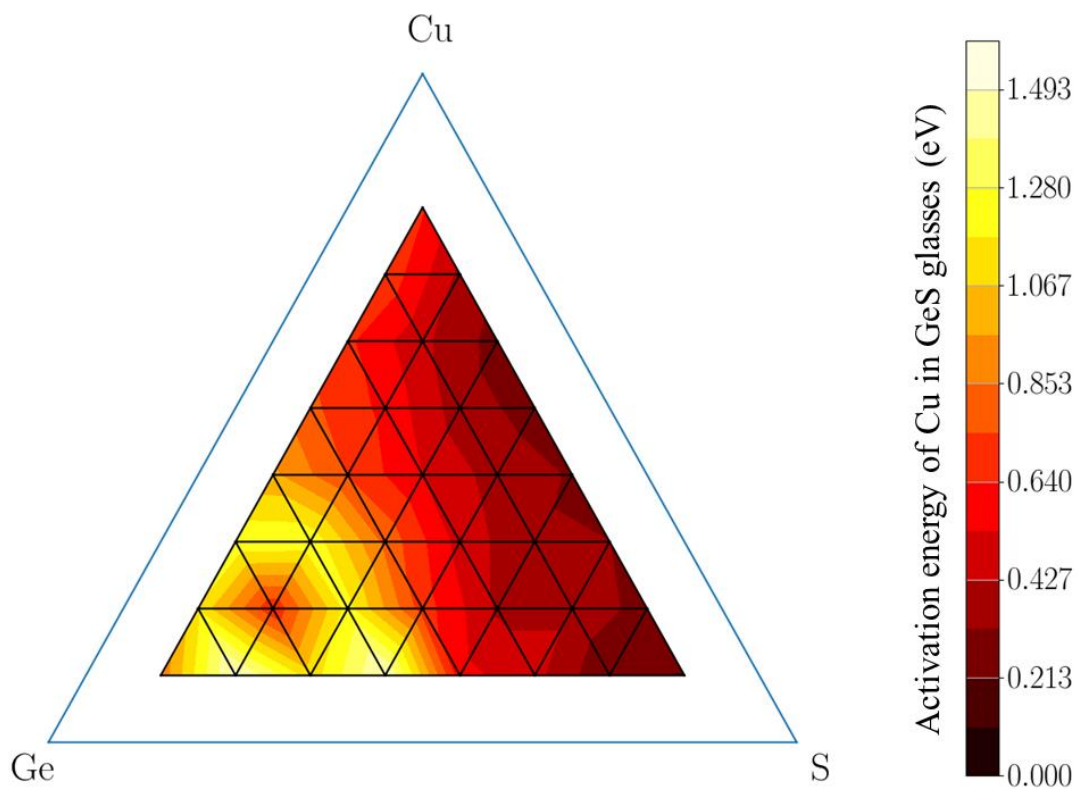


Figure 5.2. Ternary diagram for activation energy of Cu diffusion in amorphous $Ge_xS_yCu_z$ at various compositions.

We found that the activation energy for Cu diffusing in germanium sulfide glasses



reduced when increasing the content of sulfur atom and the activation energy in germanium-rich compositions is higher than sulfur-rich compositions due to their chemically-driven densification [28]. In addition, the higher activation energy in Cu-rich compositions than sulfur-rich compositions can be explained by the cluster size of Cu in the glass. When the content of Cu is larger than 60%, most of the copper atoms tend to form a large cluster and the diffusivity of Cu will reduce. Compositions with more than 70% of sulfur have low Cu activation energy and, $\text{Ge}_{0.1}\text{S}_{0.8}\text{Cu}_{0.1}$ represents the composition with the lowest activation energy of 0.21 eV. Interestingly, we also found that the compositions $\text{Ge}_{0.1}\text{S}_{0.3}\text{Cu}_{0.6}$ and $\text{Ge}_{0.1}\text{S}_{0.4}\text{Cu}_{0.5}$ have low activation barrier for Cu diffusion around 0.28 eV. Figure 5.3 shows the averaged coordination number distribution of Cu in amorphous $\text{Ge}_{0.1}\text{S}_{0.8}\text{Cu}_{0.1}$ and $\text{Ge}_{0.1}\text{S}_{0.4}\text{Cu}_{0.5}$.

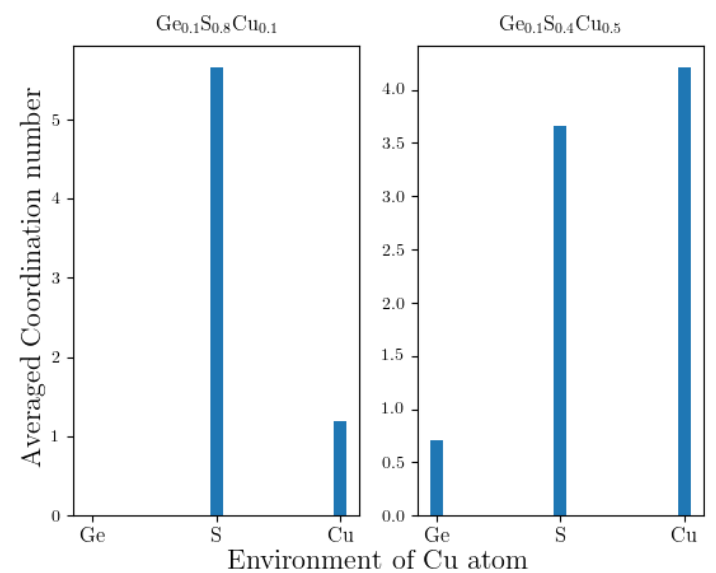


Figure 5.3. Averaged coordination number distribution of Cu atoms at glassy $\text{Ge}_{0.1}\text{S}_{0.8}\text{Cu}_{0.1}$ and $\text{Ge}_{0.1}\text{S}_{0.4}\text{Cu}_{0.5}$.

We found that the total averaged coordination number of Cu in glassy $\text{Ge}_{0.1}\text{S}_{0.8}\text{Cu}_{0.1}$ is 6.83. Moreover, 82.66 and 17.34 % of the total averaged coordination number originate from S and Cu atoms respectively. Moreover, the total averaged coordination number of Cu in glassy $\text{Ge}_{0.1}\text{S}_{0.4}\text{Cu}_{0.5}$ is 8.57 corresponding to 8.21, 42.67 and 49.1 % of Ge, S and Cu atoms, respectively.

5.3.2 Electronic bandgap

Figure 5.4. shows the value of the electronic band gap of $\text{Ge}_x\text{S}_y\text{Cu}_z$ for the compositions presented in the ternary diagram.

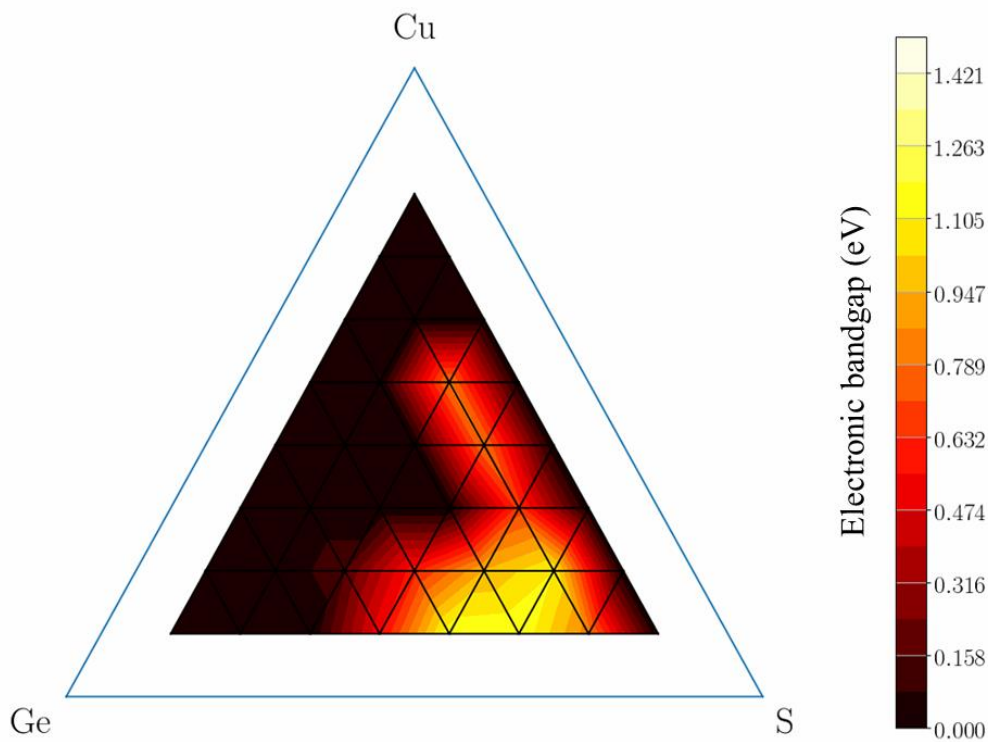


Figure 5.4. Ternary diagram for electronic bandgap of amorphous $\text{Ge}_x\text{S}_y\text{Cu}_z$ at various compositions

Based on our results, we found metallic properties for the majority of compositions corresponding to $\text{Cu} > 40\%$ and $\text{S} < 30\%$. Semiconducting compositions with bandgap

ranging from 0.15 eV to 1.18 eV were found otherwise. We selected 3 compositions at various Cu content with a fixed ratio of Ge and S. Figure 5.5. shows the total and partial density of states projected on germanium, sulfur and copper atoms for $\text{Ge}_{0.3}\text{S}_{0.6}\text{Cu}_{0.1}$, $\text{Ge}_{0.2}\text{S}_{0.4}\text{Cu}_{0.4}$ and $\text{Ge}_{0.1}\text{S}_{0.2}\text{Cu}_{0.7}$ glasses.

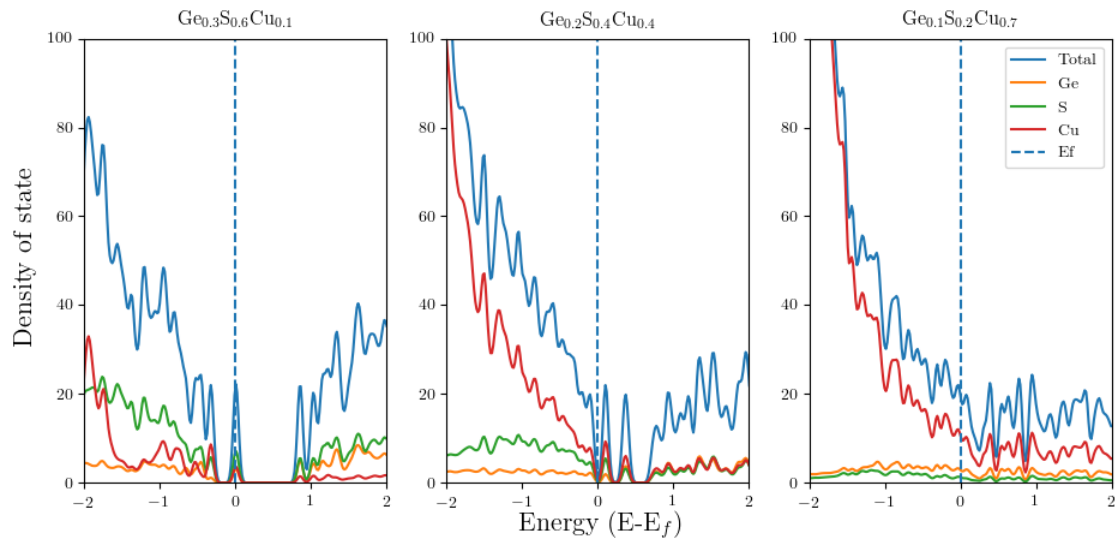


Figure 5.5. Total and partial density of state projected on germanium, sulfur and copper atoms for $\text{Ge}_{0.3}\text{S}_{0.6}\text{Cu}_{0.1}$, $\text{Ge}_{0.2}\text{S}_{0.4}\text{Cu}_{0.4}$ and $\text{Ge}_{0.1}\text{S}_{0.2}\text{Cu}_{0.7}$ glasses. The Fermi energy (E_f) has been shifted to zero for all compositions.

We found that the Fermi energy level shifts toward to the valance band when increasing copper content. The valance band overlaps with the conduction band when further rising the copper concentration. In addition, we found that most of the density of state near the Fermi energy level comes from S and Cu atoms.

5.3.3 The normalized cluster size of copper

Figure 5.6. shows the normalized Cu cluster size of $\text{Ge}_x\text{S}_y\text{Cu}_z$ for the compositions presented in the ternary diagram.

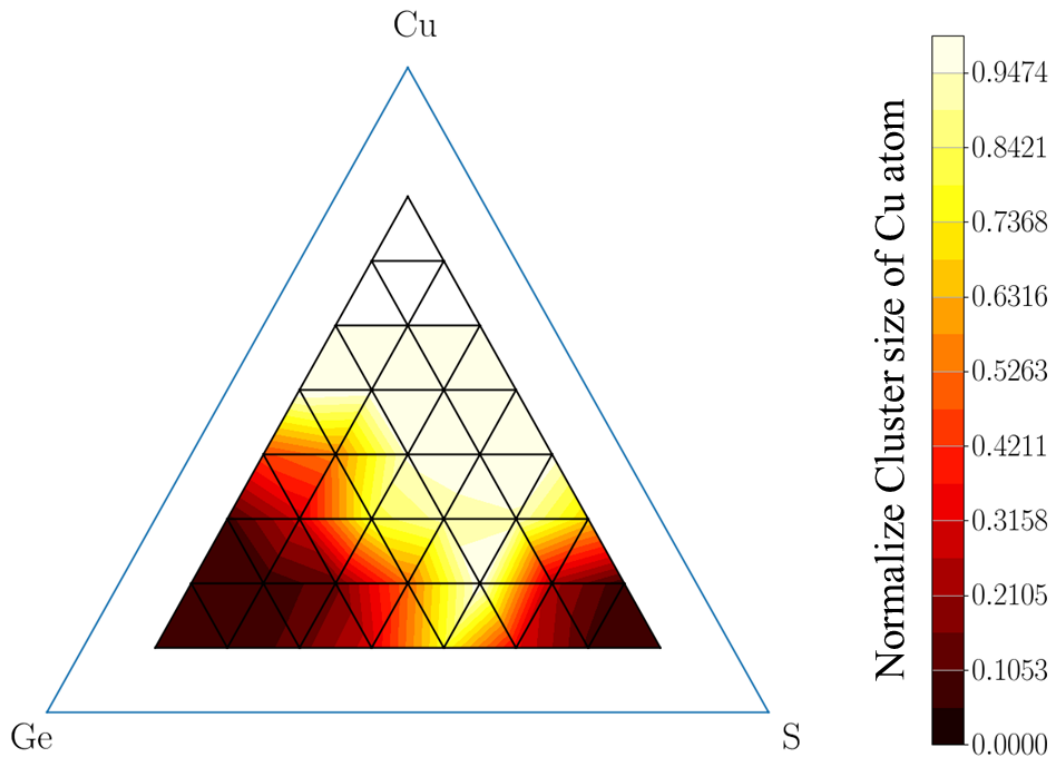


Figure 5.6. Ternary diagram for a normalized cluster size of Cu in amorphous $Ge_xS_yCu_z$ at various compositions

We found that compositions with Ge > 60% and S > 70% are composed of small Cu clusters. Figure 5.7 shows the atomic configuration for selected compositions.

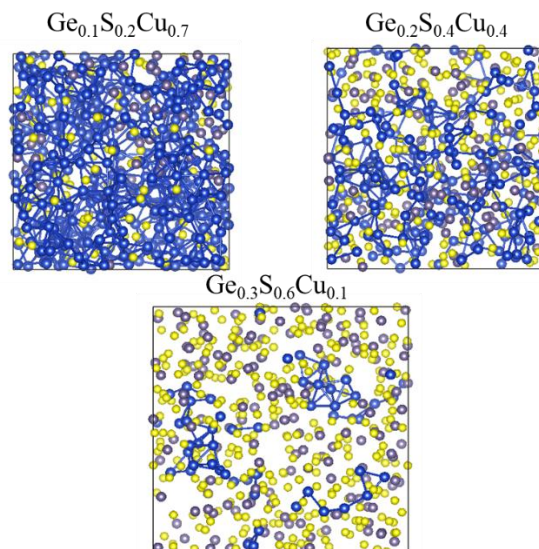


Figure 5.7. Atomic configuration and Normalized cluster size of Cu atom for $Ge_{0.3}S_{0.6}Cu_{0.1}$, $Ge_{0.2}S_{0.4}Cu_{0.4}$ and $Ge_{0.1}S_{0.2}Cu_{0.7}$ glasses.



We found that the normalized cluster size of Cu atoms is increasing with the content of copper. In addition, most of the compositions with Cu > 50% show that nearly all Cu atoms form a large cluster in the glassy germanium sulfide glasses consistent with previous work [25].



Chapter 6 Conclusions and Future work

6.1 Conclusions

To conclude, we have developed the new empirical ReaxFF for GeS/Cu based on a training set including EOS for crystals, PES for molecules and binding energy for amorphous structure and clusters by Monte Carlo optimization algorithm. We have generated an ensemble of glassy $\text{Ge}_x\text{S}_y\text{Cu}_z$ structures at various compositions by using ReaxFF to evaluate activation energy for diffusion of copper in the germanium sulfide glasses, electronic band gap and normalized cluster size of Cu. The lowest activation barrier for Cu diffusion is found for the composition $\text{Ge}_{0.1}\text{S}_{0.8}\text{Cu}_{0.1}$. Interestingly, we found low activation barrier for the Copper-rich compositions $\text{Ge}_{0.1}\text{S}_{0.4}\text{Cu}_{0.5}$ and $\text{Ge}_{0.1}\text{S}_{0.3}\text{Cu}_{0.6}$. In addition, we found the metallic properties for the majority of compositions with $\text{Cu} > 40\%$ and $\text{S} < 30\%$. Other compositions were found mostly semiconducting with bandgap ranging from 1.93 eV and 3.18 eV. We also found Cu atom often aggregate to form a cluster for the compositions with larger than 50% of Cu contents. In addition, we found that the total averaged coordination number for Cu atoms in $\text{Ge}_{0.1}\text{S}_{0.8}\text{Cu}_{0.1}$ composition is 6.83 and around 83 % and 17 % of coordination number contributed by Cu-S and Cu-Cu respectively. In our work, we have explored an interesting region of compositions for ultrafast switching ECM cells and TS. However, the amorphous Ge-S binary and Ge-S-Cu ternary structures generated by the force field



are still defective for describing the environment of Sulfur and bond length including Ge-S and Ge-Cu. It can be attributed to the highly defective amorphous structures generated by DFT based on PBE functional in the training set and fix general parameters for Ge, Cu and S in the force field during the optimizations.

6.2 Future work

In our future work, we will further explore the compositions for resistance switching in order to locate more specific region for ECM cells and TS. Moreover, we will compute the electronic properties again after further optimization for ReaxFF based on HSE functional so as to predict the more accurate value of the electronic band gap. Therefore, we will perform simulations for demonstrating the operation of the resistance switching in ECM cells with interesting compositions in order to evaluate switching time and retention on actual devices by using electrochemical dynamics with implicit degrees of freedom method [91]. This method is able to provide an accurate description of electrochemical reactions under an applied voltage based on solving the diffusion equation of external electrochemical potential contributed by each metallic atom during the reactive simulations. In addition, the experiments for demonstrating switching with 2D materials has studied. However, the atomistic mechanism is still not well understood. With Regard to this, we will explore the switching mechanism of ECM cells made of 2D materials solid electrolyte (GeS and GeS₂).



References

- [1] W. Lu and C. M. Lieber, "Nanoelectronics from the bottom up," (in English), *Nature Materials*, vol. 6, no. 11, pp. 841-50, Nov 2007 2007.
- [2] J. Markoff, "Smaller, faster, cheaper, over: the future of computer chips," *New York Times*, 2015.
- [3] R. Waser and M. Aono, "Nanoionics-based resistive switching memories," *Nature materials*, vol. 6, no. 11, pp. 833-840, 2007.
- [4] B. Jacob, S. Ng, and D. Wang, *Memory systems: cache, DRAM, disk*. Morgan Kaufmann, 2010.
- [5] D. Klein. (2010). *A complete system approach to NAND in Computing*.
- [6] G. W. Burr *et al.*, "Phase change memory technology," *Journal of Vacuum Science & Technology B, Nanotechnology and Microelectronics: Materials, Processing, Measurement, and Phenomena*, vol. 28, no. 2, pp. 223-262, 2010.
- [7] I. Valov, R. Waser, J. R. Jameson, and M. N. Kozicki, "Electrochemical metallization memories—fundamentals, applications, prospects," *Nanotechnology*, vol. 22, no. 25, p. 254003, 2011.
- [8] K. Wang, J. Alzate, and P. K. Amiri, "Low-power non-volatile spintronic memory: STT-RAM and beyond," *Journal of Physics D: Applied Physics*, vol. 46, no. 7, p. 074003, 2013.
- [9] R. S. Shenoy *et al.*, "MIEC (mixed-ionic-electronic-conduction)-based access devices for non-volatile crossbar memory arrays," *Semiconductor Science and Technology*, vol. 29, no. 10, p. 104005, 2014.
- [10] J. J. Yang, D. B. Strukov, and D. R. Stewart, "Memristive devices for computing," *Nature nanotechnology*, vol. 8, no. 1, p. 13, 2013.
- [11] S. Yu and P.-Y. Chen, "Emerging memory technologies: Recent trends and prospects," *IEEE Solid-State Circuits Magazine*, vol. 8, no. 2, pp. 43-56, 2016.
- [12] F. Zhuge *et al.*, "Mechanism for resistive switching in chalcogenide-based electrochemical metallization memory cells," *AIP Advances*, vol. 5, no. 5, p. 057125, 2015.
- [13] E. Bychkov, "Superionic and ion-conducting chalcogenide glasses: Transport regimes and structural features," *Solid State Ionics*, vol. 180, no. 6-8, pp. 510-516, 2009.
- [14] W. Chen, H. Barnaby, and M. Kozicki, "Volatile and non-volatile switching in Cu-SiO₂ programmable metallization cells," *IEEE Electron Device Letters*, vol. 37, no. 5, pp. 580-583, 2016.
- [15] Y. Yang, P. Gao, S. Gaba, T. Chang, X. Pan, and W. Lu, "Observation of



- conducting filament growth in nanoscale resistive memories," *Nature communications*, vol. 3, p. 732, 2012.
- [16] I. Valov *et al.*, "Atomically controlled electrochemical nucleation at superionic solid electrolyte surfaces," *Nature materials*, vol. 11, no. 6, pp. 530-535, 2012.
- [17] A. Wedig *et al.*, "Nanoscale cation motion in TaOx, HfOx and TiOx memristive systems," *Nature nanotechnology*, vol. 11, no. 1, p. 67, 2016.
- [18] A. Zakery and S. Elliott, "An introduction to chalcogenide glasses," *Optical Nonlinearities in Chalcogenide Glasses and Their Applications*, pp. 1-28, 2007.
- [19] P. G. Debenedetti and F. H. Stillinger, "Supercooled liquids and the glass transition," *Nature*, vol. 410, no. 6825, p. 259, 2001.
- [20] E. Bychkov, M. Miloshova, D. Price, C. Benmore, and A. Lorriaux, "Short, intermediate and mesoscopic range order in sulfur-rich binary glasses," *Journal of non-crystalline solids*, vol. 352, no. 1, pp. 63-70, 2006.
- [21] M. Celino *et al.*, "First-principles molecular dynamics study of glassy GeS₂: Atomic structure and bonding properties," *Physical Review B*, vol. 88, no. 17, p. 174201, 2013.
- [22] A. Zeidler *et al.*, "Establishing the structure of GeS₂ at high pressures and temperatures: a combined approach using x-ray and neutron diffraction," *Journal of Physics: Condensed Matter*, vol. 21, no. 47, p. 474217, 2009.
- [23] S. Blaineau, P. Jund, and D. A. Drabold, "Physical properties of a GeS₂ glass using approximate ab initio molecular dynamics," *Physical Review B*, vol. 67, no. 9, p. 094204, 2003.
- [24] S. Le Roux and P. Jund, "Influence of the cooling rate on the glass transition temperature and the structural properties of glassy GeS₂: an ab initio molecular dynamics study," *Journal of Physics: Condensed Matter*, vol. 19, no. 19, p. 196102, 2007.
- [25] D. M. Guzman and A. Strachan, "Structural and electronic properties of copper-doped chalcogenide glasses," *Physical Review Materials*, vol. 1, no. 5, p. 055801, 2017.
- [26] A. Bouzid, S. Le Roux, G. Ori, M. Boero, and C. Massobrio, "Origin of structural analogies and differences between the atomic structures of GeSe₄ and GeS₄ glasses: A first principles study," *The Journal of chemical physics*, vol. 143, no. 3, p. 034504, 2015.
- [27] S. Chakraborty, P. Boolchand, and M. Micoulaut, "Structural properties of Ge-S amorphous networks in relationship with rigidity transitions: An ab initio molecular dynamics study," *Physical Review B*, vol. 96, no. 9, p. 094205, 2017.
- [28] A. Bychkov, G. J. Cuello, S. Kohara, C. J. Benmore, D. L. Price, and E. Bychkov, "Unraveling the atomic structure of Ge-rich sulfide glasses," *Physical*



- Chemistry Chemical Physics*, vol. 15, no. 22, pp. 8487-8494, 2013.
- [29] I. Petri and P. Salmon, "A neutron diffraction study of glassy GeS₂," *Journal of non-crystalline solids*, vol. 293, pp. 169-174, 2001.
- [30] S. Blaineau, S. Le Roux, and P. Jund, "Ab initio molecular dynamics study of GeS₂: from the crystal to the glass," *Journal of Physics: Condensed Matter*, vol. 19, no. 45, p. 455207, 2007.
- [31] E. Bychkov, V. Tsegelnik, Y. Vlasov, A. Pradel, and M. Ribes, "Percolation transition in Ag-doped germanium chalcogenide-based glasses: conductivity and silver diffusion results," *Journal of non-crystalline solids*, vol. 208, no. 1-2, pp. 1-20, 1996.
- [32] W. Lu, K.-H. Kim, T. Chang, and S. Gaba, "Two-terminal resistive switches (memristors) for memory and logic applications," in *Proceedings of the 16th Asia and South Pacific Design Automation Conference*, 2011, pp. 217-223: IEEE Press.
- [33] L. Fumagalli, C. M. Lazzari, and V. Soncini, "Materials and components in phase change memory devices," ed: Google Patents, 2018.
- [34] W. Devulder *et al.*, "Influence of carbon alloying on the thermal stability and resistive switching behavior of copper-telluride based CBRAM cells," *ACS applied materials & interfaces*, vol. 5, no. 15, pp. 6984-6989, 2013.
- [35] S. R. Elliott, "Chalcogenide Phase-Change Materials: Past and Future," *International Journal of Applied Glass Science*, vol. 6, no. 1, pp. 15-18, 2015.
- [36] Micron. (2015, 26 July). *Breakthrough nonvolatile memory technology*. Available: <https://newsroom.intel.com/news-releases/intel-and-micron-produce-breakthrough-memory-technology/>
- [37] H. H. Li, Y. Chen, C. Liu, J. P. Strachan, and N. Davila, "Looking ahead for resistive memory technology: A broad perspective on rram technology for future storage and computing," *IEEE Consumer Electronics Magazine*, vol. 6, no. 1, pp. 94-103, 2017.
- [38] N. Onofrio, D. Guzman, and A. Strachan, "Atomic origin of ultrafast resistance switching in nanoscale electrometallization cells," *Nature materials*, vol. 14, no. 4, p. 440, 2015.
- [39] F. Simanjuntak, B. Pattanayak, C.-C. Lin, and T.-Y. Tseng, "Peroxide Induced Volatile and Non-volatile Switching Behavior in ZnO-based Electrochemical Metallization Memory Cell," *Nanotechnology*, 2017.
- [40] M. N. Kozicki, M. Balakrishnan, C. Gopalan, C. Ratnakumar, and M. Mitkova, "Programmable metallization cell memory based on Ag-Ge-S and Cu-Ge-S solid electrolytes," in *Non-Volatile Memory Technology Symposium, 2005*, 2005, pp. 7 pp.-89: IEEE.



- [41] M. N. Kozicki and M. Mitkova, "Mass transport in chalcogenide electrolyte films—materials and applications," *Journal of non-crystalline solids*, vol. 352, no. 6, pp. 567-577, 2006.
- [42] T. Fujii, M. Arita, Y. Takahashi, and I. Fujiwara, "In situ transmission electron microscopy analysis of conductive filament during solid electrolyte resistance switching," *Applied Physics Letters*, vol. 98, no. 21, p. 212104, 2011.
- [43] C.-J. Kim *et al.*, "Characterization of silver-saturated Ge–Te chalcogenide thin films for nonvolatile random access memory," *Journal of Vacuum Science & Technology B: Microelectronics and Nanometer Structures Processing, Measurement, and Phenomena*, vol. 24, no. 2, pp. 721-724, 2006.
- [44] C. Schindler, S. C. P. Thermadam, R. Waser, and M. N. Kozicki, "Bipolar and Unipolar Resistive Switching in Cu-Doped SiO_2 ," *IEEE Transactions on Electron Devices*, vol. 54, no. 10, pp. 2762-2768, 2007.
- [45] H. Sun *et al.*, "Direct observation of conversion between threshold switching and memory switching induced by conductive filament morphology," *Advanced Functional Materials*, vol. 24, no. 36, pp. 5679-5686, 2014.
- [46] S. Prakash, S. Asokan, and D. Ghare, "A guideline for designing chalcogenide-based glasses for threshold switching characteristics," *IEEE Electron Device Letters*, vol. 18, no. 2, pp. 45-47, 1997.
- [47] D. Ielmini, S. Ambrogio, and S. Balatti, "Stress-Induced Asymmetric Switching and Filament Instability in Electrochemical Memories," *ECS Transactions*, vol. 64, no. 8, pp. 169-175, 2014.
- [48] H.-W. Ahn *et al.*, "Effect of density of localized states on the ovonic threshold switching characteristics of the amorphous GeSe films," *Applied Physics Letters*, vol. 103, no. 4, p. 042908, 2013.
- [49] A. Padilla *et al.*, "On the origin of steep I – V nonlinearity in mixed-ionic-electronic-conduction-based access devices," *IEEE Transactions on Electron Devices*, vol. 62, no. 3, pp. 963-971, 2015.
- [50] S. Murugavel and S. Asokan, "Local structure and electrical switching in chalcogenide glasses," *Physical Review B*, vol. 58, no. 6, p. 3022, 1998.
- [51] P. Hohenberg and W. Kohn, "Inhomogeneous electron gas," *Physical review*, vol. 136, no. 3B, p. B864, 1964.
- [52] P. A. Dirac, "Note on exchange phenomena in the Thomas atom," in *Mathematical Proceedings of the Cambridge Philosophical Society*, 1930, vol. 26, no. 3, pp. 376-385: Cambridge University Press.
- [53] D. M. Ceperley and B. Alder, "Ground state of the electron gas by a stochastic method," *Physical Review Letters*, vol. 45, no. 7, p. 566, 1980.
- [54] R. M. Martin, *Electronic structure: basic theory and practical methods*.



- Cambridge university press, 2004.
- [55] A. D. Becke, "Density-functional exchange-energy approximation with correct asymptotic behavior," *Physical review A*, vol. 38, no. 6, p. 3098, 1988.
- [56] K. Burke, J. P. Perdew, and Y. Wang, "Derivation of a generalized gradient approximation: The PW91 density functional," in *Electronic Density Functional Theory*: Springer, 1998, pp. 81-111.
- [57] J. P. Perdew, K. Burke, and M. Ernzerhof, "Generalized gradient approximation made simple," *Physical review letters*, vol. 77, no. 18, p. 3865, 1996.
- [58] A. D. Becke, "A new mixing of Hartree–Fock and local density-functional theories," *The Journal of chemical physics*, vol. 98, no. 2, pp. 1372-1377, 1993.
- [59] J. Heyd, G. E. Scuseria, and M. Ernzerhof, "Hybrid functionals based on a screened Coulomb potential," *The Journal of Chemical Physics*, vol. 118, no. 18, pp. 8207-8215, 2003.
- [60] E. Artacho *et al.*, "The SIESTA method; developments and applicability," *Journal of Physics: Condensed Matter*, vol. 20, no. 6, p. 064208, 2008.
- [61] F. Neese, "The ORCA program system," *Wiley Interdisciplinary Reviews: Computational Molecular Science*, vol. 2, no. 1, pp. 73-78, 2012.
- [62] J. Hafner, "Ab-initio simulations of materials using VASP: Density-functional theory and beyond," *Journal of computational chemistry*, vol. 29, no. 13, pp. 2044-2078, 2008.
- [63] P. Giannozzi *et al.*, "QUANTUM ESPRESSO: a modular and open-source software project for quantum simulations of materials," *Journal of physics: Condensed matter*, vol. 21, no. 39, p. 395502, 2009.
- [64] F. Weigend, M. Häser, H. Patzelt, and R. Ahlrichs, "RI-MP2: optimized auxiliary basis sets and demonstration of efficiency," *Chemical physics letters*, vol. 294, no. 1-3, pp. 143-152, 1998.
- [65] M. J. Field, P. A. Bash, and M. Karplus, "A combined quantum mechanical and molecular mechanical potential for molecular dynamics simulations," *Journal of Computational Chemistry*, vol. 11, no. 6, pp. 700-733, 1990.
- [66] D. Frenkel and B. Smit, *Understanding molecular simulation: from algorithms to applications*. Academic press, 2001.
- [67] L. A. Girifalco and V. G. Weizer, "Application of the Morse potential function to cubic metals," *Physical Review*, vol. 114, no. 3, p. 687, 1959.
- [68] L. Verlet, "Computer" experiments" on classical fluids. I. Thermodynamical properties of Lennard-Jones molecules," *Physical review*, vol. 159, no. 1, p. 98, 1967.
- [69] M. Baskes, "Application of the embedded-atom method to covalent materials: a semiempirical potential for silicon," *Physical review letters*, vol. 59, no. 23, p.



- 2666, 1987.
- [70] S. L. Mayo, B. D. Olafson, and W. A. Goddard, "DREIDING: a generic force field for molecular simulations," *Journal of Physical chemistry*, vol. 94, no. 26, pp. 8897-8909, 1990.
- [71] B. W. Dodson, "Development of a many-body Tersoff-type potential for silicon," *Physical Review B*, vol. 35, no. 6, p. 2795, 1987.
- [72] K. D. Nielson, A. C. van Duin, J. Oxgaard, W.-Q. Deng, and W. A. Goddard, "Development of the ReaxFF reactive force field for describing transition metal catalyzed reactions, with application to the initial stages of the catalytic formation of carbon nanotubes," *The Journal of Physical Chemistry A*, vol. 109, no. 3, pp. 493-499, 2005.
- [73] J. Yu, S. B. Sinnott, and S. R. Phillpot, "Charge optimized many-body potential for the Si / SiO₂ system," *Physical Review B*, vol. 75, no. 8, p. 085311, 2007.
- [74] T. P. Senftle *et al.*, "The ReaxFF reactive force-field: development, applications and future directions," *NPJ Computational Materials*, vol. 2, p. 15011, 2016.
- [75] A. K. Rappe and W. A. Goddard III, "Charge equilibration for molecular dynamics simulations," *The Journal of Physical Chemistry*, vol. 95, no. 8, pp. 3358-3363, 1991.
- [76] A. Buch, "Pure metals properties: a scientific and technical handbook," 1999.
- [77] M. Grundman, "The Physics of Semiconductors: An Introduction Including Nanophysics an Applications," *XXXVII*, vol. 864, pp. 883-6, 2010.
- [78] W. J. Hehre, R. Ditchfield, and J. A. Pople, "Self-consistent molecular orbital methods. XII. Further extensions of gaussian-type basis sets for use in molecular orbital studies of organic molecules," *The Journal of Chemical Physics*, vol. 56, no. 5, pp. 2257-2261, 1972.
- [79] R. Prasher, "Thermal interface materials: historical perspective, status, and future directions," *Proceedings of the IEEE*, vol. 94, no. 8, pp. 1571-1586, 2006.
- [80] A. Becke, "AD Becke, *J. Chem. Phys.* 98, 5648 (1993)," *J. Chem. Phys.*, vol. 98, p. 5648, 1993.
- [81] D. J. Evans and B. L. Holian, "The nose-hoover thermostat," *The Journal of chemical physics*, vol. 83, no. 8, pp. 4069-4074, 1985.
- [82] S. Kirkpatrick, "Optimization by simulated annealing: Quantitative studies," *Journal of statistical physics*, vol. 34, no. 5-6, pp. 975-986, 1984.
- [83] N. Onofrio, D. Guzman, and A. Strachan, "The dynamics of copper intercalated molybdenum ditelluride," *The Journal of chemical physics*, vol. 145, no. 19, p. 194702, 2016.
- [84] G. Psogiannakis and A. C. Van Duin, "Development of a ReaxFF reactive force field for Si/Ge/H systems and application to atomic hydrogen



- bombardment of Si, Ge, and SiGe (100) surfaces," *Surface Science*, vol. 646, pp. 253-260, 2016.
- [85] J. Yeon, H. L. Adams, C. E. Junkermeier, A. C. Van Duin, W. T. Tysoe, and A. Martini, "Development of a ReaxFF Force Field for Cu/S/C/H and Reactive MD Simulations of Methyl Thiolate Decomposition on Cu (100)," *The Journal of Physical Chemistry B*, vol. 122, no. 2, pp. 888-896, 2017.
- [86] S. Plimpton, P. Crozier, and A. Thompson, "LAMMPS-large-scale atomic/molecular massively parallel simulator," *Sandia National Laboratories*, vol. 18, p. 43, 2007.
- [87] D. Chandler, "Introduction to modern statistical mechanics," *Introduction to Modern Statistical Mechanics*, by David Chandler, pp. 288. Foreword by David Chandler. Oxford University Press, Sep 1987. ISBN-10: 0195042778. ISBN-13: 9780195042771, p. 288, 1987.
- [88] S. Le Roux and V. Petkov, "ISAACS—interactive structure analysis of amorphous and crystalline systems," *Journal of Applied Crystallography*, vol. 43, no. 1, pp. 181-185, 2010.
- [89] G. Ceder and K. Persson, "The Materials Project: A Materials Genome Approach," ed, 2010.
- [90] H. Takebe, H. Maeda, and K. Morinaga, "Compositional variation in the structure of Ge–S glasses," *Journal of non-crystalline solids*, vol. 291, no. 1-2, pp. 14-24, 2001.
- [91] N. Onofrio and A. Strachan, "Voltage equilibration for reactive atomistic simulations of electrochemical processes," *The Journal of chemical physics*, vol. 143, no. 5, p. 054109, 2015.